**Universidade de Aveiro** Departamento de Física
**Ano** 2015/2016

**DANIEL JORGE PIRES JALÓ**

# Caracterização estrutural e ótica de nanofios de GaAs dopados com Mg e o impacto da funcionalização de nanoparticulas de Au

# Structural and optical characterization of Mg doped GaAs nanowires and the impact of the functionalization with Au nanoparticles

**Universidade de Aveiro** Departamento de Fisica
**Ano** 2015/2016

**DANIEL JORGE PIRES JALÓ**

# Caracterização estrutural e ótica de nanofios de GaAs dopados com Mg e o impacto da funcionalização de nanoparticulas de Au

# Structural and optical characterization of Mg doped GaAs nanowires and the impact of the functionalization with Au nanoparticles

Dissertação apresentada à Universidade de Aveiro para cumprimento dos requisitos necessários à obtenção do grau de Mestre em Engenharia Física, realizada sob a orientação científica da Prof. Doutora Rosário Correia (orientadora), Professora Auxiliar do Departamento de Física da Universidade de Aveiro, e do Prof. Doutor Joaquim Leitão (co-orientador), Professor Auxiliar do Departamento de Física.

i3N
INSTITUTO DE NANOESTRUTURAS, NANOMODELAÇÃO E NANOFABRICAÇÃO
INVESTIGAÇÃO, INOVAÇÃO E APLICAÇÕES DE ENGENHARIA

Este trabalho foi desenvolvido no âmbito do projeto i3N — Instituto de Nanoestruturas, Nanomodelação e Nanofabricação (Refª. FCT UID/CTM/50025/2013), financiado por fundos nacionais através da FCT/MEC e quando aplicável cofinanciado pelo FEDER, no âmbito do acordo de parceria PT2020.

Dedico este trabalho à minha mãe e ao meu pai, por tudo.

**o júri**

| | |
|---|---|
| presidente | Prof. Doutor António Cunha<br>Professor auxiliar do departamento de Física da Universidade de Aveiro |
| arguente | Prof. Doutor Kevin O'Donnell<br>Professor of Semiconductor Spectroscopy SUPA Physics Department<br>Strathclyde University Glasgow G4 0NG Scotland, UK. |
| orientadora | Prof. Doutora Rosário Correia<br>Professora auxiliar do departamento de Física da Universidade de Aveiro |

**agradecimentos**

À Professora Rosário Correia, que me guiou, acompanhou e apoiou durante todo este trabalho e sem a qual não o teria conseguido terminar. Obrigado pelo privilégio de trabalhar consigo, pela paciência, pela disponibilidade e pelo vasto conhecimento cientifico que adquiri como consequência de trabalhar consigo. Agradeço também ainda por me ter ajudado a realizar parte deste trabalho na Escócia.

Ao Professor Joaquim Leitão, a quem também devo a realização desta tese. Obrigado por me ter orientado, ter sempre a porta aberta e por ter partilhado a sua aprofundada experiência em semicondutores comigo.

I would like to thank Professor Kevin O'Donnell, who warmly received and guided me for five months, for his availability and immense knowledge which he kindly shared with me.

I would like to thank Prof. Manuel Silva, Gillian Craig and Prof. Yu Chen, who were kind enough to assist me with the synthesis of gold nanorods and functionalization of the GaAs nanowires.

I would like to thank Professor Paul Edwards and António Cunha for assisting me and giving me their time while performing scanning electron microscopy.

À minha família e à Chita, pelo apoio incondicional que me ofereceram durante toda a minha vida.

A todos os amigos que fiz durante o meu percurso académico e que enriqueceram estes meus últimos cinco anos.

**palavras-chave**

GaAs, nanofios, nanotecnologia, semicondutores, espectroscopia, fotoluminescência, fotoluminescência de excitaçao, catodoluminescência, Raman, nanoparticulas, nanovaras, funcionalização, efeito de carga de imagem.

**resumo**

O presente trabalho teve como objetivos principais: i) estudar o efeito da dopagem com Mg nas propriedades óticas e estruturais de nanofios de GaAs crescidos em substratos de Si(111); ii) avaliar as modificações nas propriedades óticas dos nanofios em resultado da funcionalização com nano varetas metálicas de ouro.

No estudo foram utilizadas várias técnicas de caracterização: a microscopia eletrónica de varrimento, espetroscopia de Raman, fotoluminescência, excitação da fotoluminescência e catodoluminescência. Independentemente da concentração do dopante, os resultados experimentais da espetroscopia de Raman confirmaram a coexistência das fases de blenda de zinco (BZ) e de wurtzite (WZ) ao longo do eixo de crescimento dos nanofios. Espectroscopia de fotoluminescência revelou emissões abaixo da energia de hiato do GaAs na fase BZ. A natureza indireta das emissões, característica de um alinhamento tipo II das bandas eletrónicas da BZ e WZ, foi confirmada pela dependência da energia do máximo de emissão com a raiz cúbica da potência de excitação ($P^{1/3}$). Os resultados experimentais da dependência da intensidade de PL com a potência revelaram que as emissões principais observadas são compatíveis com os modelos de recombinação de portadores *free-to-bound* ou a pares dador-aceitador na amostra menos dopada, e recombinações de excitões ligados a impurezas na amostra mais dopada. Os resultados de catodoluminescência, à temperatura ambiente, confirmaram a existência de diferentes emissões ao longo do eixo de crescimento dos fios, confirmando o politipismo estrutural. As emissões observadas em catodoluminescência concordam com as principais componentes identificadas em fotoluminescência. No estudo da fotoluminescência com a temperatura foram identificados diferentes canais de desexcitação não radiativa, cujos elevados valores de energias de ativação são consistentes com nanofios contendo segmentos muito finos de BZ. A funcionalização dos fios com nanovaretas metálicas de Au conduziu a um pequeno desvio para o azul na localização energética do máximo de emissão, mostrando que é possivel modificar as propriedades óticas dos nanofios de GaAs.

**keywords**

GaAs, nanowires, nanotechnology, semiconductors, spectroscopy, photoluminescence, photoluminescence excitation, cathodoluminescence, Raman, nanoparticles, nanorods, functionalization, image charge effect.

**abstract**

The main goals of the present work are: i) to study the impact of Mg doping on the optical and structural properties of GaAs nanowires grown on Si(111) substrates; ii) to investigate the changes in the nanowires' optical properties resulting from their functionalization with gold nanorods.

Several characterization techniques were employed during this work: scanning electron microscopy and Raman, photoluminescence, photoluminescence excitation and cathodoluminescence spectroscopy. Raman spectroscopy confirmed the coexistence of the zincblende (ZB) and wurtzite (WZ) along the nanowire's growth axis in both samples, independently of the Mg doping concentration. Photoluminescence spectroscopy showed emissions below the bandgap energy of ZB GaAs. The spatial indirect nature of the emissions, characteristic of a type II lineup of electronic bands, was confirmed from the dependence of the emission peak's energy with the cubic root of the excitation power ($P^{1/3}$). The experimental results from the PL intensity dependency with power revealed the main emissions observed to be compatible with models of free-to-bound and donor-to-acceptor pairs recombinations for the sample with higher concentration of Mg doping, and bound excitons recombinations for the sample with lower concentration of Mg doping. The samples' cathodoluminescence, measured at room temperature, confirmed the existence of different emissions along the nanowires' axes of growth, serving as further evidence of their structural polytypism. These emissions also showed to be in good accordance with the main components identified in the samples' photoluminescence. The study of the PL dependency with temperature shed light on the different non-radiative deexcitation channels, whose high activation energies are consistent with nanowires comprising very thin ZB segments. The functionalization of the nanowires with gold nanorods leads to a small blueshift of the emission peak's energy, thus showing that it is possible to alter the nanowires' optical properties.

# Contents

# List of Figures

# List of Tables

# 1 Introduction

In recent years one-dimensional semiconductor nanowires (NWs) have attracted growing interest and become one of the most active research fields within the nanoscience community. Their high surface-to-volume ratio and novel electronic, photonic, thermal, electrochemical and mechanical properties, differing from those seen in their bulk counterparts, make them ideal materials for the fabrication of nanoscale electronic and optoelectronic devices such as p-n junction light-emitting diodes, inverters, nanoscale field-effect transistors and solar cells. All of this leads to them being seen as the building blocks for the next generation of optical, sensing, electronic and energy harvesting devices [15, 16].

The advance and improvement of the growth techniques available nowadays allow for the controllable synthesis of large quantities of high quality nanowires, with most of them being synthesized out of semiconductors from the III-V and II-VI group [17]. Among these, Gallium Arsenide has shown to be particularly interesting due to its direct bandgap and high carrier mobility. Additionally, these physical properties can be further improved through the growth of the nanowires as heterostructures, something easily achievable in GaAs since it has two distinct crystalline phases that may coexist along the nanowires' axes when grown under the appropriate conditions. When that is the case, the crystalline structure in GaAs nanowires alternates between cubic zinc-blende (ZB) and hexagonal wurtzite (WZ), resulting in what is effectively a sequence of quantum disks along the nanowire.

Another interesting and seemingly unrelated class of materials has also been the focus of extensive research from the nanoscience community: noble metal nanoparticles. A source of awe and amazement since Roman times, their optical properties and the possibility of modifying them with elements from various chemical groups have made them popular for several applications such as biotechnology, targeted drug delivery and electronic storage systems [18]. Recent progress in this field and a deeper understanding of their plasmonic properties has also shed light to how the intensity of luminescence in light emitting materials can be improved by binding metal nanoparticles to them [19]. In such cases the photoluminescence enhancement originates from the coupling of the nanoparticles' plasmons with the emissions taking place in its vicinity when the frequency of these emissions matches that of the resonant modes of the nanoparticles. Recently it has been found that another mechanism exists originating not from plasmonic resonance but from electrostatic interactions instead, through which an improvement in luminescence is also possible. This mechanism was interpreted using the well known "image charge method", for which reason it is named as image charge effect, and it has the distinct advantage of not requiring resonant interactions [20].

The aim of this work is to join together these two promising materials and study them individually and together, deepening our understanding about the optical properties of polytypic Mg doped GaAs nanowires and investigating the impact that binding metal nanoparticles to the nanowires has on these optical properties. Two samples grown under different conditions and with different Mg doping concentrations were used, and the structural and optical characterization of both were carried out using different techniques, namely a scanning electron microscope, photoluminescence, photoluminescence excitation, cathodoluminescence and Raman scattering spectroscopy. Solutions of free standing gold nanorods were synthesized through the seed-mediated growth method and later added to both samples. After the functionalization of the samples all the aforementioned characterization techniques were employed again in order to determine the changes in physical properties resultant from the presence of gold nanorods.

# 2 Gallium Arsenide overview

Gallium Arsenide is a compound semiconductor which was once labelled as "the semiconductor of the future" [21]. Despite the difficulties in its fabrication and the high costs of production which kept it from dominating the semiconductor market, GaAs still enjoys success in stable niche markets. In this section the properties of GaAs in both bulk and nanowire forms will be reviewed.

## 2.1 Bulk GaAs crystal structure

Gallium Arsenide is a III-V semiconductor composed of Ga and As. Together, they crystallize into a face-centred cubic (FCC) lattice, with a basis of two atoms, one of Ga and one of As. The basis vector $\vec{b}$ is

$$\vec{b} = \frac{a}{4}\left(\hat{e}_x + \hat{e}_y + \hat{e}_z\right)$$

where $\hat{e}_x$, $\hat{e}_y$ and $\hat{e}_z$ are the cartesian unit vectors and $a$ the lattice constant. This crystal structure is more commonly known as the ZB structure, and it has a total of eight atoms within it, each connected to four atoms of the opposite species in such a way that they form a tetrahedron with the atom in its centre (fig. 2.2a). The connections are made through partially covalent bonds.

The reciprocal lattice of a ZB lattice is a body centred cubic (BCC) lattice, whose first Brillouin zone and its points of high symmetry can be seen in fig. 2.2b. The directions from the centre of the Brillouin zone, $\Gamma$ at $(0,0,0)$, towards the boundary points $X$ at $(1,0,0)$, $L$ at $(\frac{1}{2},\frac{1}{2},\frac{1}{2})$ and $K$ at $(0,\frac{3}{4},\frac{3}{4})$, are the most important ones to describe the electronic band structure of the material [3].

The lattice parameter has been widely studied and is known to depend on many factors such as the material's temperature, purity, stoichiometry and the presence or absence of dislocations. For perfect undoped GaAs at a temperature of 300 K the lattice parameter is $a_0 = 0.56535$ nm [22].

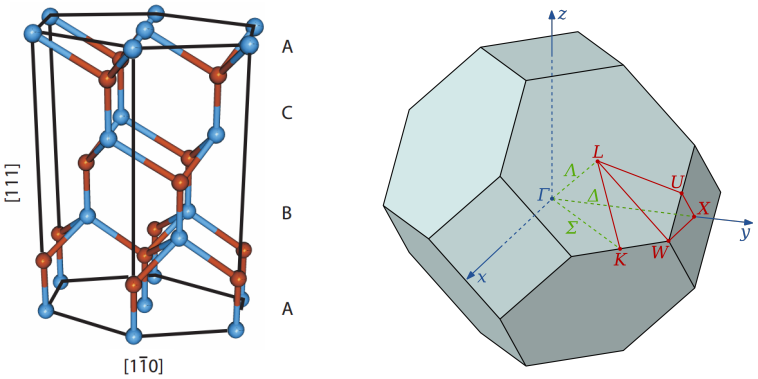


**(a)** **(b)**

**Figure 2.1:** (a) GaAs ZB crystal structure with the Ga atoms in blue and the As atoms in orange, and (b) the respective Brillouin zone with its high symmetry points and directions (adapted from [1, 2]).

## 2.2 Electronic band structure

The electronic band structure of solids allows us to study their optical and electrical properties, describing the range of allowed and forbidden energies for the electrons within the material as a function of the wave vector $\vec{k}$. GaAs, similarly to the other semiconductors of the III-V group, has a direct bandgap, with both the valence band maximum and the conduction band minimum at the centre of the Brillouin zone (Γ point), meaning that optical transition can occur that require neither emission nor absorption of phonons as the electron's momentum remains constant. This is particularly important for optoelectronic applications since the lack of energy dissipation through lattice vibrations reflects itself into more efficient devices [23]. Fig. 2.2 illustrates the bulk GaAs band structure obtained through a nonlocal empirical-pseudopotential method [24].

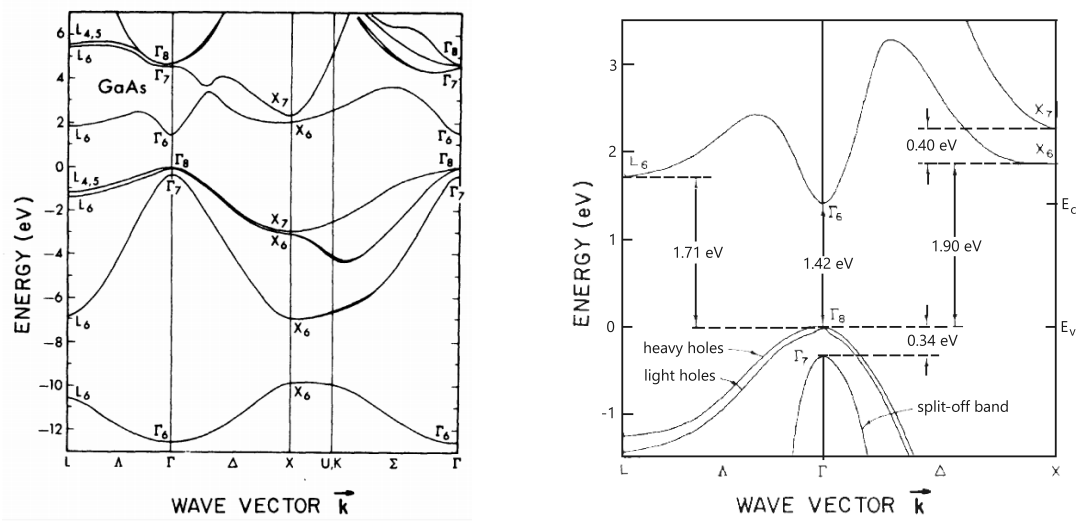


**(a)** **(b)**

**Figure 2.2:** (a) The band structure of bulk GaAs along high symmetry directions and (b) a detailed view around the high symmetry point Γ at the centre of the Brillouin zone for a temperature of 300 K (adapted from [3, 4]).

Besides the main $\Gamma_6 - \Gamma_8$ transition across the bandgap, other important ones near the Brillouin zone centre include the three indirect transitions $L_6 - \Gamma_8$, $X_6 - \Gamma_8$ and $X_7 - \Gamma_8$ which require either the absorption or emission of a phonon. At high temperatures the $L_6 - \Gamma_8$ transition will be the most intense, in part because of the higher energies involved in the $X_6 - \Gamma_8$ and $X_7 - \Gamma_8$ transitions whose energy increases quicker with temperature than that of the $L_6 - \Gamma_8$ transition.

At 300 K bulk GaAs has a direct bandgap of 1.42 eV, while the indirect transitions will have an energy of 1.71 eV, 1.90 eV and 2.30 eV, in order of increasing energy of the points $L_6$, $X_6$ and $X_7$. Its high bandgap proves to be an advantage compared to alternative small bandgap semiconductors, such as Si, since electrons won't be as easily thermally promoted across the bandgap, allowing GaAs to keep its semiconductor characteristics until higher temperatures [25].

Another important feature of its band structure is the fact that three valence bands have their maximum at Γ, with two of them, the light-hole and heavy-hole bands, having a degenerate extrema. Despite their degeneracy and both being parabolic near Γ the different curvature of the bands leads to holes with different effective masses. The remaining valence band at Γ, named split-off band, stems from the spin-orbit interaction and has its maximum slightly below the heavy and light hole bands.

## 2.3 GaAs nanowires

Nanowires are nanostructures with diameters of the order of the nanometer and a high length-to-width ratio. This one dimensional nature can lead to carrier confinement along all but one dimension of the nanowire as long as the diameter is low enough. The threshold width below which confinement effects are significant is equal to the Bohr radius, which, for GaAs, varies between ~2 nm and ~11 nm.

Opposite to most semiconductors, GaAs and a few other III-As compound semiconductors can adopt a hexagonal WZ structure (fig. 2.3a) when grown as a nanowire under favourable conditions, instead of the cubic ZB structure observed in their bulk form. Furthermore, the coexistence of both the ZB and the WZ phases along single nanowires' axes is commonly observed (fig. 2.3b), a phenomenon known as polytypism [26, 27]. The growth conditions that lead to the crystallization in one structure over the other aren't fully known yet despite the topic having been studied and discussed by several authors [28–30]. Nevertheless, factors such as the ionicity of the compound, the radii of the nanowire and the pressures and temperatures under which it was grown are known to influence the way the semiconductor crystallizes .

A polytypic material is comprised of structurally similar individual layers within which two-dimensional translations are preserved. The phenomenon itself arises from the way these individual layers are stacked within the crystal structure. In the case of GaAs, the two possible crystal phases differ in the stacking of the bilayers of III-V pairs that compose the crystal: while a ZB lattice has an ABCABC stacking sequence, WZ lattices follow an ABABAB stacking sequence. Therefore stacking defects such as stacking faults or planar defects introduce a WZ bilayer in a ZB segment or vice-versa (e.g. a stacking fault turns a purely ZB region, ABCABCABC, into a ZB region with a WZ segment, ABCABABC).

The presence of the two different crystalline structures, each with different properties, results in unique additional properties of the nanowire as a whole. The different band structure, for example, leads to a non-constant band allignment and consequently additional confinement of the carriers. There have been many different theoretical and experimental attempts to determine the bandgap of WZ GaAs, however this task has proven to be quite challenging due to the difficulties

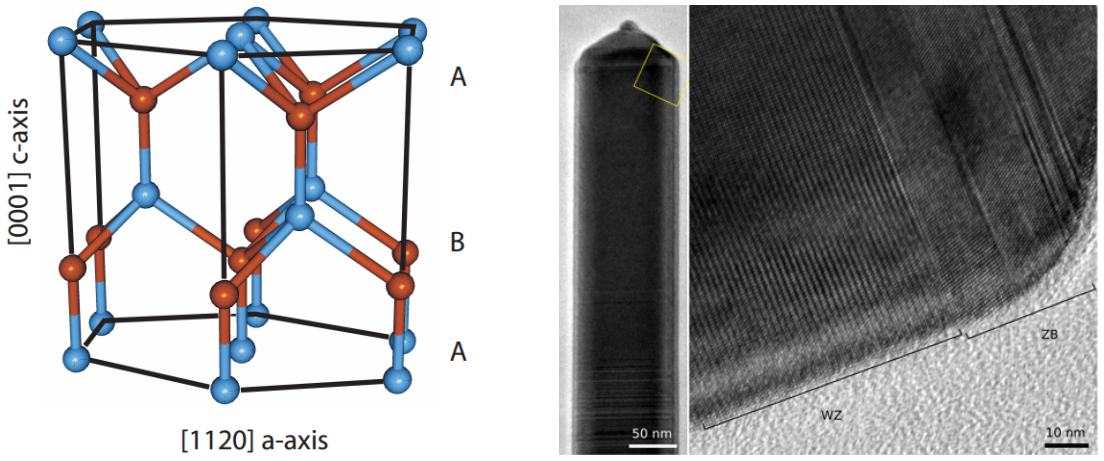


**(a)** **(b)**

**Figure 2.3:** (a) Hexagonal WZ unit cell with Ga atoms in blue and As atoms in orange, and (b) HRTEM images of a GaAs where polytypism between ZB and WZ phases is present along its axis (adapted from [5]).

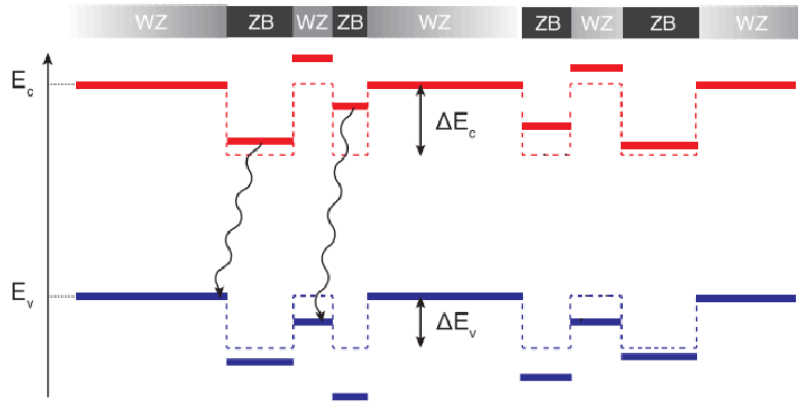


**Figure 2.4:** Qualitative model of the band allignment seen along the axis of a GaAs nanowire composed of alternating WZ and zincblende phases. The solid and dashes lines correspond to the bands' energies when confinement is and isn't considered, respectively. Only interband transitions between carriers trapped in ZB segments and carriers trapped in WZ segments are shown. Intraband transitions within the same phase are also possible despite their lower probability of taking place (adapted from [6]).

in the growth of WZ GaAs thin films. As of now, no consensus has been reached and its exact value remains still somewhat unknown with most authors proposing values ranging from 1.46 eV to 1.56 eV [31–37]. Most authors tend to agree however that both conduction and valence bands of WZ GaAs have energies greater than those of the ZB phase. Despite the exact offset being also under debate, theoretical calculations have suggested it lays between 76-122 meV for the valence bands and 53-117 meV for the conduction bands [1, 17, 38]. If the nanowire's diameter is large enough that lateral quantum confinement effects are negligible, then the nanowire can be seen as a sequence of multiple non-periodic and irregular quantum wells, with the energy band alignment being that of a staggered type II band lineup (fig. 2.4). We can thus expect to observe spatially indirect recombinations between electrons and holes trapped into adjacent quantum wells. Because of the lower overlap between the wave functions of the electrons and holes the relaxation time should be greater than that of spatially direct transitions.

Electrons and holes are confined in different wells and therefore their confinement energies should be considered separately. Since holes' effective mass is lower than electrons', their confinement energy for a well of equal width will always be lower to that of electrons'. For GaAs the value of the electron's effective mass is $m_e$ ~0.067 $m_0$, where $m_0$ is the free electron mass. Meanwhile the effective mass of the holes is $m_{lh}$ ~0.09 $m_0$ or $m_{hh}$ ~0.34 $m_0$ for the most common situation in quantum wells, depending on whether the hole is in the light-hole or heavy-hole valence band [39].

The optical, structural and electrical properties of GaAs nanowires also depend on their doping profile. In the case of GaAs the most used p-type dopant is beryllium, however its high toxicity and carcinogenic attributes has lead to a search for alternatives. Among all the possibilities Mg, which replaces the Ga atom creating a shallow acceptor level in bulk GaAs with an estimated ionization energy of 28 meV [40], shows to be one of the most promising. Despite some complications in the doping of GaAs with Mg arising from its low incorporation coefficient, different studies on Mg doped GaAs nanowires have been reported [41, 42].

# 3 Gold nanoparticles

Metal nanoparticles (NPs) have been the focus of intensive research in the last decades due to their interesting properties. These include their high surface-to-volume ratio and ability to scatter and absorb light with extraordinary efficiency [43, 44]. Furthermore, various controllable factors, such as their shape, size, external environment, aggregation and composition, influence their final properties, which means that the NPs' properties can be tuned and optimized for specific applications [45].

It is also seen that when a light emitting material is in the vicinity of metal NPs an improvement of its luminescent properties is possible due to two separate mechanisms: localized plasmon resonance and image charge effect, both of which will be described in detail below.

## 3.1 General properties

For as long as humanity can remember gold has been regarded as one of the most precious materials on Earth. Historically, this is mostly due to its use as a currency, while its use in industrial settings has been quite low due to the existence of cheaper alternatives. Nevertheless, gold's good electrical and thermal conductivity, ability to be applied as very thin films and its non-reactive nature lead to its use in niche applications within different industries, particularly electronics [46].

With the growth of the field of nanotechnology a renewed interest around metal NPs, specially gold and silver ones, has emerged. These NPs have actually been used as early as fourth century during the Roman empire (the famous Lycurgus cup is a good example of how the use of gold NPs gave the vessel unique optical properties when hit by light [47], even though the reasons for such odd properties were unknown at the time). Nowadays metal NPs are of great usefulness and their number of applications are growing rapidly due to intense ongoing research. They were found to have important value in the fields of: medicine and biology, where metal NPs are used as a tool to diagnose and treat a number of diseases [43, 48], sensor industry, acting as building blocks of sensing devices in various fields [49], and solar cell technology, where gold NPs are responsible for trapping light and increasing the cell's efficiency [50].

## 3.2 Localized surface plasmons

Many of the applications of metal NPs come from their unique interaction with light at low dimensions. When a NP is exposed to light whose wavelength is considerably greater than the NP's dimensions a collective coherent oscillation of free electrons takes place as a result of the incident light's electric field, displacing the free electrons cloud away from the nuclei and leading to the emergence of a restoring force between the two in the form of Coulomb attraction [45], as is illustrated in figure 3.1 for a spherical NP [7]. The electron cloud's oscillation results in a dipole oscillation along the direction of the electric field of the incident light.

The oscillations described, which always take place at the interface between a conductor and an insulator, are called surface plasmons and are the source of evanescent electromagnetic waves [51]. For confined particles the oscillations are called localized surface plasmons (LSPs), and the strength of the interaction between the LSPs and the incident light will be the strongest at a specific resonant wavelength, named localized surface plasmon resonance (LSPR), whose value will depend on the NPs properties (size, shape, composition, etc) and the local refractive index in the vicinity of the NPs surface [52]. This whole phenomenon leads to a much higher absorption and

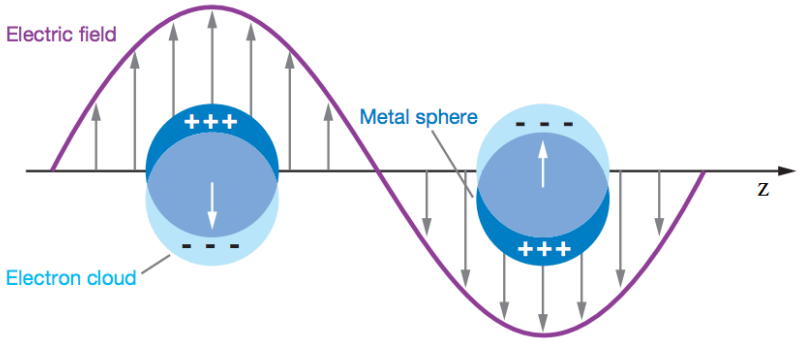


**Figure 3.1:** Schematic diagram illustrating the behavior of the electron cloud within a metal particle when subject to an electric field, also known as a localized surface plasmon (adapted from [7]).

scattering of light at the resonant wavelength than in identically sized non-metal NPs.

Let's consider the simplest case of a single spherical metal NP of radius $r$ being irradiated by an $x$-propagating, $z$-polarized light at wavelength $\lambda$. The sphere finds itself in an environment with dielectric constant $\epsilon_{out}$, while the inside of the sphere has an inner dielectric constant of $\epsilon_{in}$ highly dependent on the incident light's wavelength but not on the NP's size. The incident light's electric field $\vec{E}$ is:

$$\vec{E}(x,t) = E_z^0 cos(kx - \omega t)\hat{z} \tag{3.1}$$

where $k$ is the wave number and $\omega$ the angular frequency. Through Mie's theory [53–55], we can obtain the analytical solution to the time-dependent electric and magnetic fields as a function of position, starting from Maxwell's equations, so long we take two approximations. Firstly, we must consider that $kx << \omega t$ so that the spatial component $kx$ in eq. 3.1 can be ignored. Secondly, we must consider the wavelength to be considerably greater than the NP's radius ($r/\lambda < 0.1$), so that the electric field for distances of the order of the sphere's size are spatially independent (quasi-static field approximation). Based on this assumptions we can obtain the NP's extinction spectrum, defined as the sum of the absorption and light-scattering spectrum

$$\Upsilon(\lambda) = \frac{24\pi^2 N r^3 \epsilon_{out}^{3/2}}{\lambda \ln(10)} \left( \frac{\epsilon_i(\lambda)}{(\epsilon_r(\lambda) + \chi\epsilon_{out})^2 + \epsilon_i(\lambda)^2} \right) \tag{3.2}$$

where $\epsilon_r$ and $\epsilon_i$ are the real and imaginary part of the metal NP's dielectric constant and $\chi$ is a factor that depends on the geometry of the NP, which takes the value of 2 for a sphere but can be as high as 20 for geometries with high aspect ratios. $\chi$ can be found through analytical methods for spheres and spheroids and numerical methods for more complicated shapes [56–59]. Eq. 3.2 dictates that the absorption and scattering of light by the NP depends on its external environment, its own geometry and on the incident light's wavelength [60]. Furthermore, the extinction spectrum is also influenced from aggregation of NPs, since the electromagnetic fields of nearby NPs couple among themselves.

The aforementioned light scattering properties of the NPs can serve as a tool to increase the luminescence of light emitting materials, such as GaAs nanowires. However, for this increase to be significant a match between the frequencies of the light emitting material's luminescence and of the NPs' LSPs must occur, i.e. the two must be in resonance with each other. When this condition is met a new recombination path becomes available, which in turn will lead to a significant increase

in the number of carriers' recombinations [20]. The resultant higher luminescence can thus be explained if we look at the recombination lifetimes and the related quantum efficiency. The total recombination lifetime is:

$$\frac{1}{\tau} = \frac{1}{\tau_{rad}} + \frac{1}{\tau_{nonrad}} + \frac{1}{\tau_{plasmon}} \tag{3.3}$$

where $\tau_{rad}$ and $\tau_{nonrad}$ represent lifetimes for radiative and non radiative channels excluding plasmonic effects and $\tau_{plasmon}$ represents the lifetime of the new recombination path introduced by the LSP resonance. The latter is a radiative process and its lifetime is considerably greater than that of $\tau_{rad}$ when resonance takes place, resulting in a decrease of the total recombination lifetime. This decrease is done at the expense of the non-radiative recombinations that will decrease with respect to the radiative recombinations. All of this results in an increase in the Internal Quantum Efficiency (IQE) of the material which is defined below.

$$IQE = \frac{\tau_{rad} + \tau_{plasmon}}{\tau_{rad} + \tau_{plasmon} + \tau_{nonrad}} \tag{3.4}$$

Previous works have shown that an enhancement of up to 10× can be achieved this way, however utilizing this phenomenon in real world devices has been challenging due to the resonant frequencies requirement [52, 61–63].

## 3.3 Non-resonant light emission enhancement: image charge effect

Recently it has been found that the addition of metal NPs to semiconductors can produce PL enhancement through a mechanism other than plasmonic resonance. This new mechanism emerges instead from the carrier-metallic NP electrostatic attraction and, as its discussion relies on the "Image Charge method", received the name of Image Charge Effect, hereafter abbreviated to ICE [20]. The enhancement in photoluminescence resultant from this effect is comparable to that achieved by plasmonic interactions but with the advantage of not requiring that the NPs plasmons and the frequency of the light emitting material's emission line up.

The origin of the ICE stems from Thomson's theorem [64] that states that the equilibrium distribution of charges on the surface of an isolated conductor, such as metal NPs, corresponds to the minimum of the potential energy [65]. When applied to a neutral metal NP this theorem tells us that any set of electrical charges, such as electrons and holes contained within a semiconductor in the NP's vicinity, induces a polarization in the NP equivalent to a charge distribution within it of equal and opposite magnitude. As a result Coulomb forces will cause a drift of excited carriers towards the nearest NP.

Despite being electrically neutral the excitons also experience an attraction to neutral surfaces and, consequently, will be attracted to the NPs. For metal spheres the attraction of a single carrier of charge $q$ will be $\boldsymbol{E}(r) \sim 1/qr^5$ for large distances and $\boldsymbol{E}(r) \sim 1/q(r-R)^2$ for distances close to its surface, with $R$ standing for the NPs radius [66, 67]. The latter is strong enough to cause a permanent drift of the carriers towards the metal nanosphere and as a consequence increase the concentration of both electrons and holes in its vicinity. This leads to a greater number of recombinations in this region which reflects itself in an increase on the internal quantum efficiency mentioned earlier (eq. 3.4). This quantity can be rewritten as a function of the concentration of excited carriers, $n$, in a quantum well [68]:

$$IQE = \frac{Bn^2}{An + Bn^2 + Cn^3} \tag{3.5}$$

The coefficient A is related to Shockley–Read–Hall nonradiative recombinations, B to the probability of radiative electron-hole recombination and C to the probability of Auger recombinations involving three carriers. This last term can be neglected for our samples as its value has been estimated to be of the order of $10^{-30}$ - $10^{-31}$ $cm^{-6}s^{-1}$ for GaAs [69], which means that contributions from Auger recombinations are not significant for materials with doping concentrations of the order of $10^{17}$ $cm^{-3}$, as is the case of the GaAs nanowires studied in this work. Although both non-radiative and radiative processes depend on the excited carriers' concentration, the former depends linearly while the latter depends quadratically, and consequently as the concentration increases so does the internal quantum efficiency. The theoretical discussion presented below, which is valid for nanospheres and can be found in ref. [20], is included in this work as a way to illustrate the important factors involved in the luminescence enhancement stemming from the ICE.

The local concentration of carriers in the vicinity of a nanosphere can be obtained from the coupled nonlinear diffusion equations in the presence of the electrostatic force $q\boldsymbol{E}(r)$.

$$\frac{\partial n_e}{\partial t} = D_e \nabla^2 n_e + \frac{eD_e}{k_B T} \nabla \cdot (\boldsymbol{E} n_e) - n_e(A - Bn_h) + g \tag{3.6}$$

$$\frac{\partial n_h}{\partial t} = D_h \nabla^2 n_h + \frac{eD_h}{k_B T} \nabla \cdot (\boldsymbol{E} n_h) - n_h(A - Bn_e) + g \tag{3.7}$$

Here $n_{e/h}$ represent the concentration of electrons/holes, $D_{e/h}$ their diffusion coefficients, $e$ the elemental charge of an electron, $k_B$ the Boltzmann constant, $T$ the temperature and $g$ the density of electon-hole pairs produced by the pumping laser per second. If we linearize the previous equations in the vicinity of the nanosphere ($r - R \ll R$) we find that [65]

$$n_{e/h}(r) \propto exp\left(\frac{\gamma R}{4(r-R)}\right), \quad r > R \tag{3.8}$$

The parameter $\gamma$ defines the width of the region with higher concentration of carriers, and is given by

$$\gamma = \frac{e^2}{\epsilon k_B} \frac{1}{RT} \tag{3.9}$$

The main points to take away from this last expression is the influence of both the temperature and the dimensions of the NPs on the enhancement in luminescence: the lower both these quantities are the strongest the enhancement in luminescence is. As far as we can tell no studies have been made on the improvement in luminescence from ICE resulting from gold nanorods, the particles used in this work, instead of gold nanospheres.

Finally, another consequence of the ICE in materials with quantum wells is the energetic blueshift of the emission. This is a result of the attraction carriers feel towards the end of the well closest to the NP that in turn will provoke a phenomenon called band bending, ultimately responsible for the blueshift. The discussion of this phenomenon will be left for a later part of our work and enquadrated within our experimental results [66].

# 4 Nanostructures growth techniques

Many of today's electronic and optoelectronic devices are only possible because of the highly sophisticated growth techniques currently available. The once challenging manufacturing of low dimension materials, such as extremely pure crystal thin films, heterostructures, metal nanoparticles, and quantum wells, wires and dots, can now be achieved with high precision and reliability.

## 4.1 Molecular Beam Epitaxy

Molecular beam epitaxy (MBE) is an epitaxial growth technique whereby thin highly pure atomic layers are grown at a very slow rate on top of a monocrystalline substrate. In a typical MBE setup (fig. 4.1) the material's constituent elements are heated in separate quasi-Knudsen effusion cells until they evaporate, at which point an atomic/molecular beam, whose flux depends on the effusion cells' temperatures, will form and travel ballistically towards a highly pure substrate whose surface is free of defects. The substrate is found on a holder that rotates at a constant speed, ensuring an uniform deposition and constant layer thickness across the grown material. The holder is also equipped with a heater that keeps an uniform temperature along the substrate [70]. The chamber is kept under ultra-high vacuum to guarantee that no undesired doping of the material takes place, and the properties of the material can be tuned by controlling the material's growth conditions (substrate and effusion cells' temperature, growth time, control of the mechanical shutters of the effusion cells and so on). The growth of the material can be monitored during the process through a mass spectrometer that analyses the residual gas of the chamber and a reflection high energy electron diffraction (RHEED) arrangement that assesses the surface structure of the material.

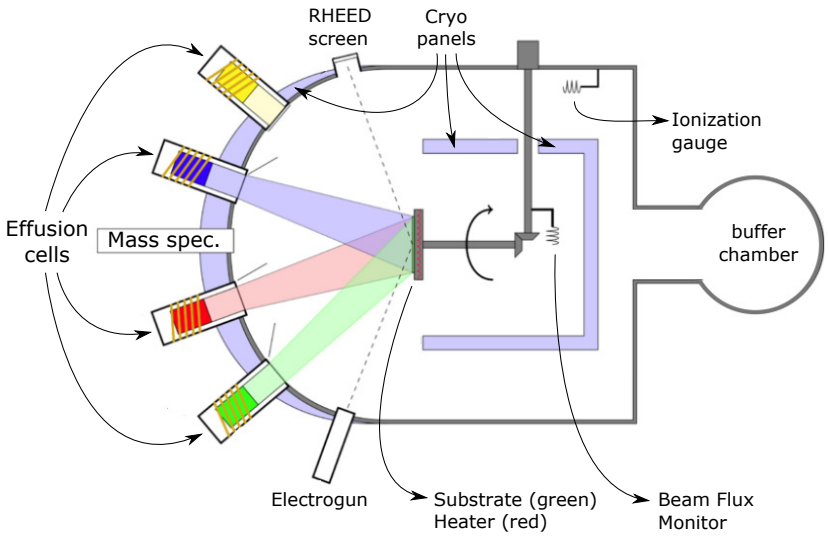


**Figure 4.1:** Schematic of a typical stainless steel cryo-pumped MBE growth chamber (adapted from [8]).

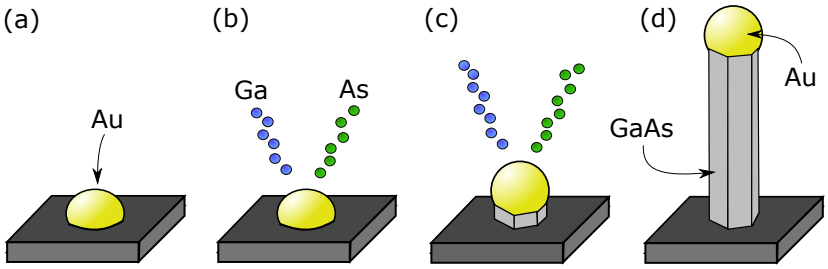


**Figure 4.2:** Illustration of the three steps of GaAs nanowires growth with the Au-assisted Vapour-Liquid-Solid mechanism as described in our text (a-c) and the end result (d).

## 4.2 Au-assisted Vapour-Liquid-Solid

The epitaxial growth of semiconductor one-dimensional nanostructures requires special care as regular growth mechanisms will result in uniform crystal structures. The growth mechanism must thus achieve a strong anisotropy, so that the growth takes place mostly along one direction, and be capable of forming individual isolated nanowires instead of a continuous structure [71]. Of the many mechanisms that fit this criteria the *particle assisted Vapour-Liquid-Solid* (VLS) is the one most widely used, typically with Au particles as the catalyst [72]. This mechanism can be described in three short steps as illustrated in fig. 4.2: first Au colloidal NPs are deposited all over the substrate's surface by means of drop-coating (fig. 4.2a). Next, the evaporated constituent elements of the nanowire are collected by the Au droplets (fig. 4.2b) until they become supersaturated, at which point the supplied species start crystallizing at the liquid-solid interface along the nanowire's axial direction (fig. 4.2c), although some lateral growth can also take place through the deposition of the evaporated species on the lateral surface of the NW. The end result of this growth mechanism is a nanowire with a leftover gold NP at the top (fig. 4.2d). The presence of the gold NP might have undesirable effects on the nanowires' properties for some electronic/optoelectronic devices (e.g. CMOS technology) [71]. As a side note, we warn the reader not to confuse these gold NPs, that result from the chosen growth mechanism of the nanowires, with the gold NPs that will be used to functionalize the nanowires and whose synthesis and functionalization process will be discussed later in this section.

### 4.2.1 Samples

The two samples studied throughout the present work, grown at the *Universidade Federal de Minas Gerais*, are composed of nanowires grown on a high quality p-type silicon substrate with a (111) surface orientation by the just described Au-assisted VLS growth mechanism on a *MBE Riber 2300 R&D* reactor. The colloidal Au droplets used as a catalyst had an average diameter of 5.0±0.5 nm, and the remaining growth parameters used for each sample follow on table 4.1.

| Sample | $T_{Mg}$ (°C) | $T_G$ (°C) | $T_{Ga}$ (°C) | $P_{As}$ (Torr) | $p_{Hall}$ ($cm^{-3}$) |
|---|---|---|---|---|---|
| **BH1114-2** | 200 | 625 | 945 | $3.8\times10^{-5}$ | $5\times10^{16}$ |
| **BH1115-2** | 220 | 617 | 945 | $3.9\times10^{-5}$ | $1\times10^{17}$ |

**Table 4.1:** Growth parameters used for the samples studied in the present work. The parameters $T_{Mg}$, $T_G$ and $T_{Ga}$ stand for the respective effusion cells' temperature, $P_{As}$ for the beam equivalent pressure of As and $p_{Hall}$ for the nominal free hole concentration determined from Hall effect measurements.

## 4.3 Functionalization of NWs with Au NPs

As previously shown, metal nanoparticles possess great value by themselves, however, among others, one of the goals of this work is to see how coupling them to GaAs nanowires will alter the wires' properties. This requires first the synthesis of NPs with the properties we desired. The seed-mediated growth method, described below, allows us to grow NPs with our desired properties that will later on be attached to the nanowires.

### 4.3.1 Synthesis of Au nanoparticles for functionalization of the NWs

When synthesizing nanoparticles it is very important that control exists over their dimensions and composition, as those will dictate the final properties of the nanoparticles. One synthesis technique that allows this control is the seed-mediated growth method through which nanorods with aspect ratios between 1.5 and 10 (surface plasmon absorption maxima between 600 nm and 1300 nm) can be grown. Compared with alternative techniques it is seen that it produces fewer undesired nanospheres ($0-1\%$) and no NPs of undesired geometries ($\phi$-shaped or Y-shaped NPs for example), as well as allowing us to control the nanoparticle's dimensions [73–78].

The seed-mediated growth method can be divided into two phases: the preparation of the seed and the preparation of the growth solution, with the latter differing depending on whether we want NRs with aspect ratios above or below 4.5 (longitudinal resonant plasmon wavelengths above or below ~850 nm). This method requires the use of hexadecyltrimethylammoniumbromide (CTAB), sodium borohydride ($NaBH_4$), ascorbic acid ($C_6H_8O_6$), chloroauric acid($HAuCl_4$) and silver nitrate ($AgNO_3$). To achieve aspect ratios greater than 4.5, benzyldimethylhexadecylammoniumchloride (BDAC) is also necessary.

The seed solution is prepared by mixing a $HAuCl_4$ (2.5 ml; 0.0005 M) solution (when dealing with the $HAuCl_4$ the lights must be dimmed down) with a CTAB solution (7.5 ml; 0.2 M) and slowly stirring it. Afterwards ice cold $NaBH_4$ (0.6 ml; 0.01 M) is added, followed by vigorous stirring for about two minutes, at which point the solution is left to rest for three hours hidden from light at room temperature.

The growth solution preparation depends on whether nanorods with aspect ratios greater or smaller than 4.5 are desired. For the former case $HAuCl_4$ (50 ml; 0.001 M) is added to a CTAB solution (50 ml; 0.2 M), turning the solution yellow/orange. $AgNO_3$ (1.875 ml; 0.004 M) is then mixed with the previous solution followed by gentle mixing, and finally ascorbic acid (700 $\mu$L; 0.0778 M) is added and the solution gently swirled, resulting in a colourless solution due to its mild reducing properties. Once both the seed and the growth solutions are ready, the former is slowly added to the latter and left to mature for one day. During this time, nanorods will form and the colour of the solution will gradually change. The key to controlling the length of the synthesized nanorods while keeping their diameter constant, thus altering their aspect ratios and the longitudinal resonant mode, is by changing the amount of $AgNO_3$ added to the sample (the nanorods used in this work, with a plasmon resonant wavelength of around 680 nm, were obtained by adding 200 $\mu$L). Greater concentrations of $AgNO_3$ will translate into nanorods of greater aspect ratios which in turn will lower the longitudinal resonant mode's energy. Only aspect ratios up to 4.5 (longitudinal resonant mode at around 850 nm) can be achieved through the aforementioned procedure, but for the purpose of our work, that is enough. Images obtained from SEM of some of the gold nanorods synthesized are shown in chapter 6 (fig. 6.3a).

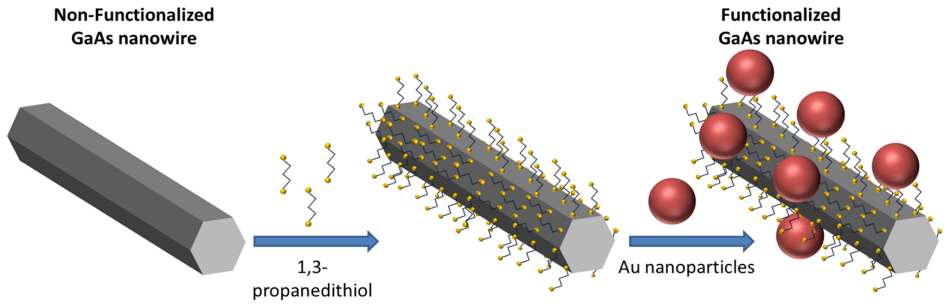


**Figure 4.3:** Illustration of the process of functionalization of nanowires with NPs, as described in our work (adapted from [9]).

### 4.3.2 Functionalization

The process through which we bind the NPs, nanorods in the present work, to the nanowires is known as functionalization [79] and can be described in two steps (fig. 4.3):

1. Assuming the sample is clean (if not it can be cleaned by passing ethanol across its surface), a few drops of a 1,3-propanedithiol/ethanol solution on a proportion of 1/10 (e.g. 100 $\mu$L of 1,3-propanedithiol to 900 $\mu$L of ethanol) should be placed on the region of the sample containing the nanowires and left to react for one hour. Afterwards the sample should be cleaned again with ethanol and left to dry.

2. Once dry, a drop of the solution containing the gold nanoparticles is deposited on the sample and left to react for one hour. Afterwards the sample should be cleaned again to remove excess chemicals, but this time distilled water is to be used instead of ethanol.

When completely dry the sample should be functionalized, and nanorods should be found attached to the surface of the nanowires. To confirm this the samples should be observed under an electron microscope capable of resolving the individual nanorods.

# 5 Experimental techniques

## 5.1 Scanning Electron Microscopy

For a long time magnified images of any material or substance could only be obtained with the use of optical microscopes. However, the fact that they operate with visible light puts some restrictions on the level of possible magnification. Scanning electron microscopes (SEMs) emerged as an alternative to circumvent this limitation as they use a focused beam of electrons instead, and consequently are capable of achieving greater magnification and resolution [80–82]. A diagram of a typical SEM is sketched in figure 5.1a.

On a SEM, the electrons are produced at the top of the column on the so called electron gun, typically a tungsten filament similar to those found in incandescent light bulbs, with a cathode and an anode charged plate in its vicinity. When current passes through the filament, causing it to heat up, electrons are released from the metal's surface, and subsequently guided through the microscope column by the two charged plates which have a small aperture on them. While the negatively charged plate will repel the electrons the positive one will have the opposite effect, and by controlling the accelerating voltage applied between the plates we can control the speed at which the electrons are emitted from the gun.

The electron gun is capable of accelerating the electrons but not of focusing them - they are emitted with a spray pattern. A system composed of electromagnetic lenses (condenser and objective lenses) is thus necessary to focus the electrons on a single spot of the sample. The condenser lens can control the size of the electron beam, which relates to the resolution of the final image, while the objective lens focuses the beam into the desired spot on the sample. The scan coils allow further control of the beam by changing its path along two perpendicular directions, ultimately allowing the scanning of the whole target area.

When the electron beam hits the target two scenarios are possible:

1. the primary electron beam collides with an electron of one of the sample's atoms, ejecting it out of its K-shell. This electron will then be captured by a secondary electron detector placed inside the sample's chamber. The amount of secondary electrons ejected is related to the sample's surface topography, e.g. a depression or dip in the sample leads to less secondary electrons being able to escape from the surface, while a bump will lead to the opposite. By scanning across the whole target area we end up with brighter and darker zones which forms a gray scale SEM image of the sample's topography;

2. the primary electron beam collides with a nucleus of a sample atom, bouncing back and being captured by the backscattered electron's detector. Since the probability of the incident electron being elastically backscattered is related to the probability of it hitting the nucleus of the sample's atoms, zones within the sample with greater atomic weight will lead to a greater number of backscattered electrons than zones with lower atomic weight. This means that the resulting image will be a representation of the density of the sample's surface, allowing the differentiation between the atoms of different elements present in the sample.

The images obtained from SEM will therefore contribute to the characterization of the given material, providing important information about its surface topography and composition. In the case of nanowires important information regarding their dimensions, shapes and geometries is also obtained.

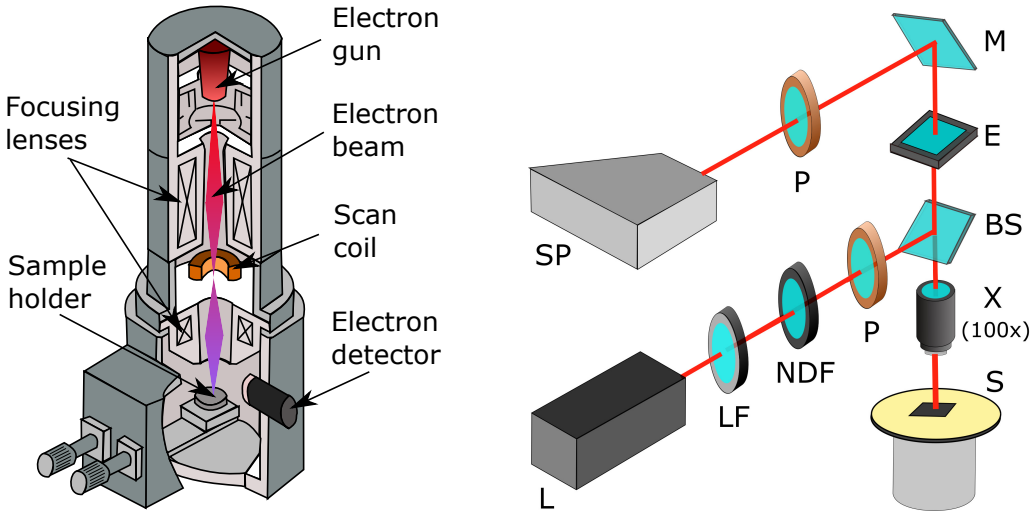


**Figure 5.1:** (a) Schematic of a typical SEM setup with its main components identified (adapted from [10]) and (b) of a Raman experiment in a backscattering configuration comprising of a light source such as a laser (L), a laser line filter (LF), a polarizer (P), a neutral-density filter (NDF), a beam splitter (BS), a microscopic lens (X), the sample on a movable platform (S), a high rejection band edge to filter out the laser light (E), a mirror (M) and a spectrometer (SP).

Finally, a SEM also has the capability of performing elemental analysis through a technique called energy dispersive X-ray spectroscopy (EDS). This technique is based on the fact that when the individual atoms of the sample are hit by the electron beam shell transitions take place, which are accompanied by the emission of X-rays. By detecting these X-rays and measuring their energies we can determine the elemental composition of the sample's surface up to a depth of 2 $\mu$m.

## 5.2 Raman spectroscopy

In solids, including low-dimension ones such as nanowires, Raman spectroscopy provides a close look into the vibrations of the crystal's lattice, i.e. phonons. These are of great importance as they reflect many of the crystal's structural properties, such as its symmetry, periodicity, phase, orientation, atomic arrangement, strain and the presence of structural defects and impurities [83, 84].

In Raman spectroscopy (fig. 5.1b) a sample is irradiated with monochromatic radiation, typically a laser. A small fraction of this incident light will be elastically scattered (Rayleigh scattering), and an even smaller fraction will be inelastically scattered (Raman scattering). A Raman experiment measures the latter and converts it into a Raman spectrum, where the intensity of the inelastically scattered light is plotted against the energy shift in respect to that of the laser light. As the intensity of the elastic scattering is several orders of magnitude greater than the inelastic scattering, a high rejection edge filter is typically included in a Raman experiment to reduce the intensity and width of the elastically dispersed contribution, otherwise the peaks of interest might find themselves buried under it.

Additionally two polarizers might be included in the experiment in order to study the polarization dependence of the Raman peaks. The first is placed in the optical pathway preceding the incidence in the sample and the second just before the detector. By orientating them in respect to

one another we can investigate how the intensity of the Raman peaks depend on different polarization configurations. This dependence might be enough to identify the spectrum's peaks in the cases where the crystal's selection rules are known from group theory.

In non-resonant conditions the intensity of any given Raman peak depends on the Raman tensor **R**, which carries the properties of the crystal's symmetry [85]:

$$I_S \propto \omega^4 I_0 |\hat{e}_s \cdot \mathbf{R} \cdot \hat{e}_i|^2 \tag{5.1}$$

where $\omega$ and $I_0$ are the frequency and intensity of the incident light, respectively, and $\hat{e}_i$ and $\hat{e}_s$ indicate the polarization of the incident and scattered light, respectively. The Porto notation $\hat{k}_i(\hat{e}_i,\hat{e}_s)\hat{k}_s$ is typically used to describe the scattering geometry of Raman experiments, with $\hat{k}_i$ and $\hat{k}_s$ representing the directions of the incident and scattered light (in a backscattering montage $\hat{k}_i = -\hat{k}_s$). The Raman tensor is a symmetric second rank tensor as long as we neglect the difference in frequency of the incoming and scattered light. Therefore, whether or not a particular phonon is active will depend on equation 5.1, from which the selection rules can be obtained.

Let's consider the case where a ZB GaAs nanowire lays perpendicular to the incident light. In such a case the light can be scattered in one of two facets: $(11\bar{2})$ and $(0\bar{1}1)$. Since scattering is more likely to happen in the $(0\bar{1}1)$ facet the set of axes most appropriate to describe the material's selection rules correspond to the directions $x_1//[0\bar{1}1]$, $x_2//[211]$ and $x_3//[\bar{1}11]$ (fig. 5.2a).

For a WZ GaAs nanowire on the other hand new scattering facets must be considered. Out of all the possibilities the $(2\bar{1}\bar{1}0)$ facet is the most appropriate one, with the corresponding axes being $x_1//[2\bar{1}\bar{1}0]$, $x_2//[01\bar{1}0]$ and $x_3//[0001]$ [85]. Rewriting the Raman tensor in the aforementioned bases allows us to calculate the selection rules of GaAs for both crystal phases.

For ZB GaAs, which crystallizes in a cubic lattice with $T_d$ symmetry, two degenerate transverse optical (TO) modes and one longitudinal optical (LO) mode are observed at the Γ point, as can be seen from the phonon dispersion plot in figure 5.2b. Both these modes are Raman active, with the former having an energy of 267 $cm^{-1}$ (TO) and the latter an energy of 291 $cm^{-1}$ (LO). As for WZ GaAs, the atoms crystallize in a hexagonal lattice with $C_{6v}$ symmetry instead. The phonon dispersion plot can be approximated by folding the ZB phonon dispersion along the [111] direction (fig. 5.2c), as the unit cell length of WZ along the [0001] is double that of the ZB's along the [111] direction. From group theory we can then predict eight phonon modes at the Γ point ($2A_1 + 2B + 2E_1 + 2E_2$), two of which are silent while the remaining, listed in table 5.1, are Raman active [11].

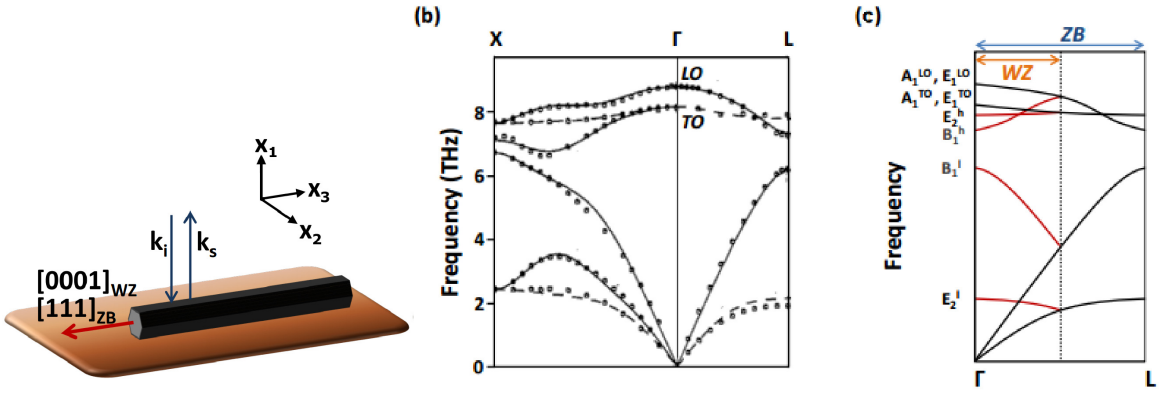


**Figure 5.2:** Schematic of the coordinate system used in relation to our nanowires' main axis (a), and the phonon dispersion for ZB GaAs (b) and WZ GaAs (c), where the red line in the latter represents the folding of the ZB phonon dispersion ((a) adapted from [11] and (b-c) from [12]).

| | Mode | Energy ($cm^{-1}$) | Referential 1 | Referential 2 |
|---|---|---|---|---|
| **ZB** | LO | 267 | $\bar{\mathbf{x}}(\mathbf{y},\mathbf{z})\mathbf{x}$, $y(x,z)\bar{y}$, $z(x,y)\bar{z}$ | ——— |
| | TO | 291 | ——— | $\bar{x_1}(x_2,-)x_1$, $\bar{x_1}(x_3,-)x_1$ |
| **WZ** | $A_1$ (LO) | 291 | $z(x,x)\bar{z}$, $z(y,y)\bar{z}$ | $\bar{x_1}(x_2,x_3)x_1$, $\bar{x_1}(x_3,x_3)x_1$ |
| | $A_1$ (TO) | Unknown | $\bar{\mathbf{x}}(\mathbf{y},\mathbf{y})\mathbf{x}$, $\bar{\mathbf{x}}(\mathbf{z},\mathbf{z})\mathbf{x}$, $y(x,x)\bar{y}$, $y(z,z)\bar{y}$ | ——— |
| | $E_1$ (TO) | 267 | $\bar{\mathbf{x}}(\mathbf{z},\mathbf{y})\mathbf{x}$, $y(x,z)\bar{y}$ | $\bar{x_1}(x_3,x_2)x_1$, $\bar{x_1}(x_2,x_2)x_1$ |
| | $E_1$ (LO) | Unknown | ——— | ——— |
| | $E_2^{L/H}$ | 59/259 | $\bar{\mathbf{x}}(\mathbf{y},\mathbf{y})\mathbf{x}$, $y(x,x)\bar{y}$, $z(x,x)\bar{z}$, $z(y,y)\bar{z}$ | $\bar{x_1}(x_2,x_2)x_1$, |

**Table 5.1:** Raman active phonon modes for ZB and WZ GaAs nanowires and their selection rules for the crystal axes ($z$ parallel to the nanowire's growth axis) (Ref. 1) and for the referential composed of the directions described in the text (Ref. 2) [13]. The modes allowed for a Raman experiment employing a backscattering configuration are highlighted in bold.

From the latter, two are also present in the ZB GaAs: $A_1$ (LO) and $E_1$ (TO). It can be shown that these two modes may mix as a consequence of the anisotropy of the force constants, resulting in two new modes $A_1$ (LO) and $E_1$ (TO) [86, 87], whose exact positions haven't been predicted or measured yet. Meanwhile, the modes $E_2^H$ and $E_2^L$ are unique to WZ GaAs and should be observable in Raman experiments.

The Raman spectra obtained throughout the experiment for GaAs nanowires will thus consist of a number of peaks, each related to its Raman active vibrational modes, i.e. those allowed by the selection rules [88]. Since we have two different possible phases for our nanowires we expect different peaks for each, which should allow us to identify different phases in the sample.

## 5.3 Photoluminescence

The emission of light by matter can take place through different mechanisms, e.g. heating (incandescence), chemical reactions (chemiluminescence), electrical current (electroluminescence), mechanical action (mechanoluminescence) among others. In our work we focus on photoluminescence (PL), where, as the name suggests, luminescence originates as a consequence of absorption of light. In semiconductors this process is started with the promotion of carriers from the ground state to an excited state as a result of photon absorption.

The radiative recombination process in semiconductors is mainly determined by transitions involving band extrema or bound states where the structure and the shape of the lowest conduction bands and of the highest valence bands are of extreme importance. In most cases this translates into an electron being excited from the valence band to the conduction band.

Once excited, the carriers will relax to a lower energy state either through radiative or non radiative paths. Various types of radiative carrier recombinations can take place in a semiconductor with the most relevant for p-doped semiconductors being (fig. 5.3a) [89–91]:

- **free exciton (FX) emission**; recombination between an electron and hole that feel an attraction to each other as a result of an electrostatic Coulomb force and, thus, form an exciton. The electrostatic interaction lowers the energy of the excited state of the crystal below that of the bandgap energy ($E_g$) by an amount $E_x$ that corresponds to the binding energy of the exciton. In the case of a direct band-gap semiconductor, the photon energy is:

$$E_{FX} = E_g - E_x \tag{5.2}$$

- **band-band (BB)**: standard recombination between the valence and conduction band. This process becomes important in not highly pure and imperfect crystals and for $k_B T > E_x$, where the formation of excitons is unlikely and the electron-hole pairs remain as free carriers that occupy the band states. In most cases this recombination involves the higher energy heavy-hole valence band, but it may also involve the light-hole/split-off valence band, albeit with lower probability;

- **band-acceptor ($eA^0$) emission**: the doping of a semiconductor introduces new impurity centres in the material. For p-doped semiconductors acceptor centres are formed that are neutral at low temperatures and lie at an energy $E_A$ above the valence band. Once electrons in the valence band acquire enough thermal energy, the charge state of acceptor defects becomes negative. After the excitation of the crystal, an electron in the conduction band can recombine with a hole bound to the defect, releasing in the process a photon of energy

$$E_{eA^0} = E_g - E_A \tag{5.3}$$

- **donor-acceptor (DA) emission**: radiative recombination between an electron bound to a donor and a hole bound to an acceptor. The unintentional doping of the sample with foreign species might result in undesired donor and acceptor impurities that often compensate each other, with the electrons of donors being captured by the acceptors. At equilibrium some of these donors and acceptors may be ionized ($D^+$ and $A^-$, respectively), and if the semiconductor is put under optical excitation electron-hole pairs that are created can be captured by the ionized donors and acceptors, neutralizing them in the process, and form a DA pair. In addition to the energetic decrease stemming from the acceptor (donor) energy levels being slightly above (below) the valence (conduction) band, a further change in

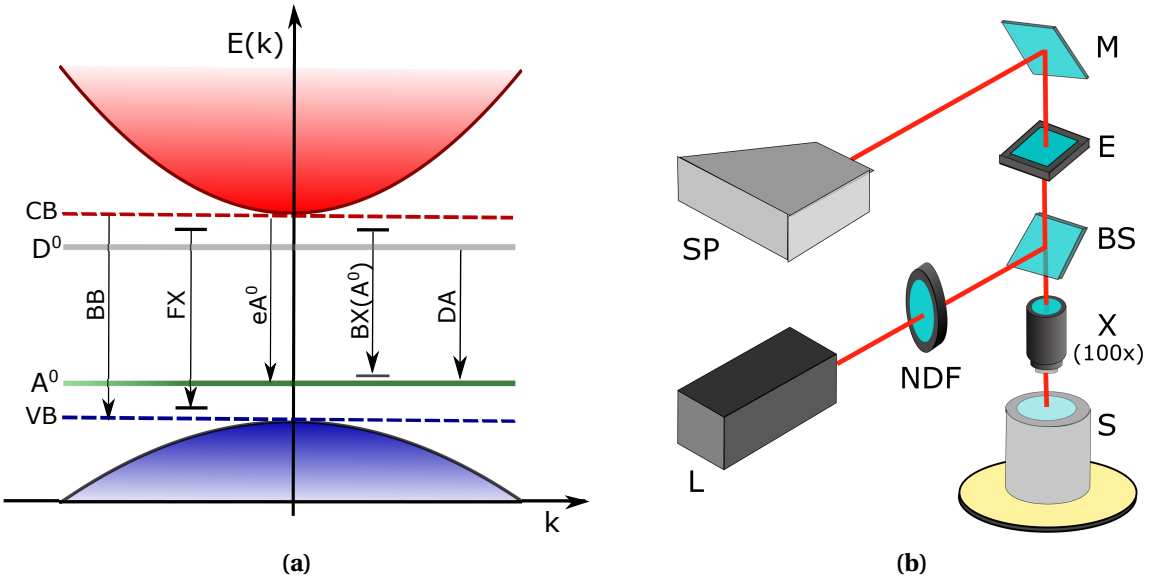


**Figure 5.3:** (a) Some of the transitions that may take place in a p-doped semiconductor such as Mg doped GaAs and (b) the experimental setup of a photoluminescence experiment with a backscattering configuration, comprising of a light source such as a laser (L), a neutral-density filter (NDF), a beam splitter (BS), a microscopic lens (X), the sample within a movable cryostat (S), a high rejection band edge (E), a mirror (M) and a spectrometer (SP).

energy will take place as a result of the Coulomb interaction between the DA pair:

$$E_{DAP} = E_g - E_A - E_D + \frac{e^2}{4\pi\epsilon_0\epsilon_r R} \tag{5.4}$$

where $R$ is the distance between the donor and acceptor impurity;

- **exciton bound to a neutral acceptor (BX($A^0$)) emission**: a free exciton is localized in a defect (most likely an acceptor impurity in p-type semiconductors). In such a case the recombination energy of the exciton is further decreased to include the new localization energy $E_{loc}$ of the trapped exciton in the defect, equal to the energy required to remove the exciton from the impurity.

$$E_{BX} = E_g - E_x - E_{loc} \tag{5.5}$$

All the above recombinations take place within a single phase and are thus spatially direct. For GaAs nanowires however additional recombination paths must be considered to accommodate for the spatially indirect transitions that result from the type II band alignment (fig. 5.4). In this type of radiative transitions, electrons are localized in ZB segments whereas holes are localized in WZ segments, as a consequence of the band alignment at the ZB/WZ interfaces discussed previously.

Properties of a material such as the electronic energy levels structure including the bandgap energy and luminescence related to point defects like, for example, impurities, can be explored through PL experiments, which are low cost (except when liquid He is required to cool the sample), non destructive and highly accurate. The experimental apparatus (fig. 5.3b) consists of an excitation light source, usually a laser, a sample holder inside a cryostat that allows the cooling of the sample, a spectrometer to measure the luminescence of the sample and an optical system composed of lenses, filters and mirrors to guide and focus the laser. If we want to reduce the source's power we can do so by placing power density filters on the incident light's path.

### 5.3.1 Temperature dependent PL

By controlling external factors, such as the temperature of the sample or the excitation power of the incident light, we can obtain additional valuable information about the sample. Temperature dependent photoluminescence, for example, gives us insight into the localized states in semiconductor materials as well as the nature of the radiative and non-radiative de-excitation channels in the sample. For semiconductors such as GaAs the transitions' energies are expected to decrease and broaden with increasing temperature as a result of the electron-phonon interaction and of the thermal expansion that the lattice undergoes as temperature increases.

The temperature dependence of the bandgap energy, $E_g$, is most commonly fitted with the three parameter empirical Varshni equation [92], however alternative equations have been proposed based on three or four parameters [93, 94]. Among those, the four parameter semi-empirical Pässler equation has proven to give a better fit at low temperatures than other existing models for several semiconductors, including GaAs. One of the four parameters model proposed by Pässler is [95]

$$E_g(T) = E_g(0) - \frac{\alpha\Theta}{2}\left(\sqrt[p]{1+\left(\frac{2T}{\Theta}\right)^p} - 1\right) \tag{5.6}$$

where $E_g(0)$ represents the bandgap energy at $0K$, $\alpha$ the limiting slope of the energy curve at high temperatures, $\Theta$ the average phonon temperature given by $\Theta \equiv \hbar\bar{w}/k_B$, $\bar{w}$ an average of phonons' energies and $p$ is an empirical parameter related to the degree of phonon dispersion of the semiconductor [95, 96].

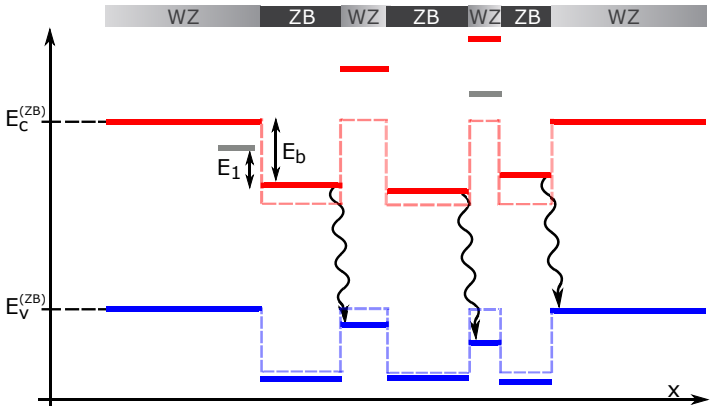


**Figure 5.4:** Energy diagram illustrating the energy levels within the multiple quantum wells and the energetic levels $E_i$ (only the state for $i = 1$ is present) and $E_b$ originating from non-radiative de-excitation mechanisms (adapted from [6]).

When the semiconductor is under light excitation the electron promoted to the conduction band will diffuse and tend to relax to a lower energy level. At low temperatures the majority of excitons find themselves bound in point defects and, some of them, end up recombining with emission of light. For the case of Si, with the increase of temperature until ~25 K, the luminescence from the free excitons can be observed with increasing temperature due to the release of excitons from shallow impurities. However, as temperature increases further previously inactive non-radiative de-excitation channels become activated and, consequently, a thermal quenching of the emission's intensity starts taking place.

The intensity dependence on temperature can be used to investigate the non radiative mechanisms present in our samples. The general equation we employ is based on two different PL quenching mechanisms that will be discussed below [97, 98].

$$I(T) = I_0 \left[ 1 + \sum_i c_i exp\left(-\frac{E_i}{k_B T}\right) + c_b T^{3/2} exp\left(-\frac{E_b}{k_B T}\right) \right]^{-1} \tag{5.7}$$

In this expression $I_0$ stands for the PL intensity at 0 K. Within the brackets we can find three terms, with the last two describing the influence of non-radiative channels in the quenching of the PL intensity (fig. 5.4). The first channel (second term in eq. 5.7) relates to the thermal activation of channels involving discrete non-radiative states of energy $E_i$ that can be either excited states of the radiative state or related to the presence of defects in the material. The parameters $c_i$ in this term are proportional to the ratio between the degenerescence of the higher energy state and of the radiative state. The second channel (third term in eq. 5.7), in the scope of our samples, corresponds to the case where the confined carriers overcome the potential barrier of energy $E_b$ from the radiative state through a non-radiative path, e.g. an electron trapped within a WZ quantum well is released to the conduction band of the adjacent ZB phase. The $T^{3/2}$ is included in order to account for the band's effective density of states, whereas the $c_B$ constant is merely a fitting parameter [99].

### 5.3.2 Power dependent PL

The excitation power dependence of the luminescence is an important tool to investigate the electronic nature of the transitions. It has been shown that for emissions taking place near the

band edge of bulk semiconductors or heterostructures the dependence of the integrated PL intensity with the power of the excitation source is linear in nature when seen on a log-log plot ($log(I)$ $vs$ $log(P)$) so long the power is kept under a range of two orders of magnitude. When that is the case this dependence takes the form of the following relationship

$$I \propto P^m \tag{5.8}$$

where $m$ is the parameter that represents the slope of the linear dependence. When the excitation laser light's energy is greater than the bandgap of the semiconductor, as is the case in this work's experiments, the parameter $m$ is expected to be less than 1 for free-to-bound and donor-acceptor pair recombinations, and between 1 and 2 for free and bound exciton recombinations [100].

## 5.4 Photoluminescence excitation spectroscopy (PLE)

Photoluminescence excitation spectroscopy is an experimental technique that looks to investigate the individual contribution of higher excited states in the process of excitation of the material that results in the population of radiative states [97, 101]. This is done by varying the excitation wavelength, usually done by pairing a Xenon lamp with a monochromator, and keeping the detection wavelength constant.

In a PLE experiment the sample is excited by photons of energy $h\nu$. The fraction $\Omega$ of light absorbed by optical centres, whose absorption coefficients is $\mu_c(\nu)$, is given by [101]

$$\Omega = \frac{\mu_c}{\mu_c + \mu_b} \tag{5.9}$$

where $\mu_b$ stands for the absorption coefficient of all the other processes not related to the optical centres. The intensity of the light absorbed by the optical centres can then be written as a function of the incident light $I_0(\nu)$, the sample thickness $d$ and the reflection coefficient $R$ [101]:

$$I_c(\nu) = I_0(\nu)\,(1-R)\,\Omega \frac{1 - exp\left(-(\mu_c + \mu_b)d\right)}{1 - R \cdot exp\left(-(\mu_c + \mu_b)d\right)} \tag{5.10}$$

The resulting spectrum will therefore measure the fraction of light from $I_c(\nu)$ that is emitted as luminescence as a function of the exciting photon's energy. This dependence can be seen as an approximation of the material's absorption spectrum from which we can investigate how each individual electronic level contributes to the emission taking place at the detection wavelength.

## 5.5 Cathodoluminescence

The phenomenon of cathodoluminescence is similar to that of photoluminescence but with a different source of excitation. Instead of light, cathodoluminescence excitation uses accelerated electrons which will promote the sample's electrons across different levels of energy. Since the SEM already provides a way to hit the sample with a focused electron beam we can use a cathodoluminescence detector within the SEM chamber to capture the resulting emitting light and study the material's optical properties. Since we are scanning over a region, exciting one point of the sample at a time, we end up with a map of spectra for each, allowing us to study how luminescence varies along the sample. This technique is particularly interesting for samples where different emissions are expected from different spots of the sample, such as is the case in polytypic nanowires.

# 6 Experimental results

## 6.1 Scanning Electron Microscope

The morphology of the samples was explored on a first approach at the University of Strathclyde on a Quanta Feg-250 high resolution environmental scanning electron microscope capable of providing a magnification up to 1000000×. It possessed a Schottky emission electron gun capable of accelerating electrons from 200 V up to 30 kV and producing a probe current as high as 200 nA. It is also equipped with an Everhardt Thornley secondary electron detector (SE), a high-contrast back-scattered electron detector (BSE) and a cathodoluminescence detector (CL). Vacuum below $6\times10^{-4}$ Pa can be produced within the SEM's chamber, although other vacuum modes are available (low vacuum and environmental SEM).

At a later stage of this work new images were obtained at the University of Aveiro, after the samples were functionalized, with a TESCAN VEGA3 SB SEM. This SEM is equipped with a tungsten heated cathode electron gun capable of achieving an accelerating voltage between 200 V and 30 kV and a probe current between 1 pA and 2 $\mu$A. Both high (<$9\times10^{-3}$ Pa) and low (3 Pa to 500 Pa) vacuum modes are available and a magnification from 3× up to 1000000× is possible. The equipment also includes an Everhart-Thornley type (YAG crystal) SE detector and a retractable annular BSE detector scintillator type (also YAG crystal), but no cathodoluminescence detector.

From a medium magnification (fig. 6.1 and 6.2) both samples studied in this work can be described as a "forest" of nanowires who possess no clear preferential orientation. However, some differences in their geometry can be seen: while the nanowires of the BH1114-2 sample show some curvature along their length, those of the BH1115-2 sample are much straighter. The differences in their geometries can be attributed to the different growth conditions under which both samples were produced.

The observed undefined orientation of the nanowires is a common problem in III-V nanowires grown on Si(111) substrates that has an impact on their integration in mainstream Si technology [102]. Its origin stems from the alloying of the Au particle with Si that leads to the formation of four {111} facets, each of which causes the nanowire to grow in a different direction. The nanowires can thus either grow perpendicularly or at an angle of 19° with the surface of the substrate [103].

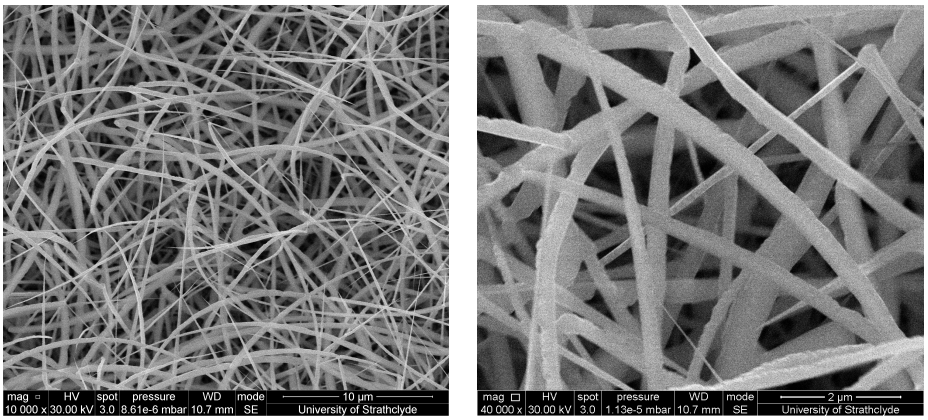


**(a)** **(b)**

**Figure 6.1:** SEM topographical view from the nanowires of sample BH1114 before functionalization obtained at a magnification of (a) 10000× and (b) 40000×.

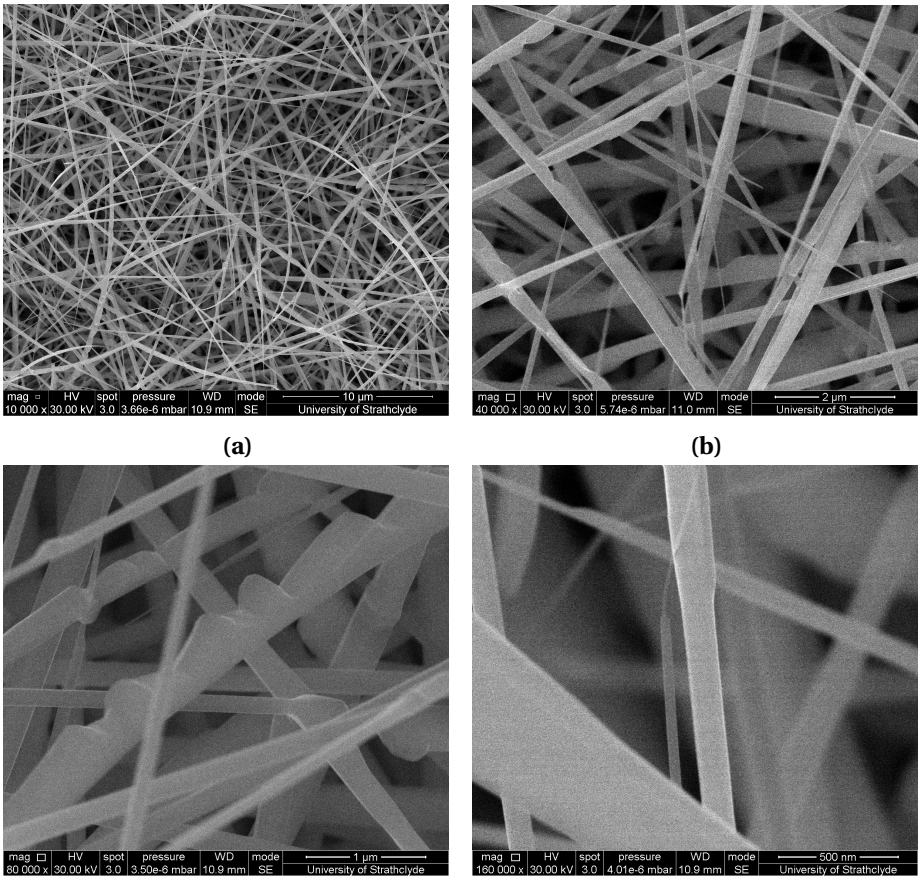


**Figure 6.2:** SEM topographical view from the nanowires of sample BH1115 before its functionalization obtained at a magnification of (a) 10000×, (b) 40000×, (c) 80000× and (d) 160000×.

The nanowires from both samples have a maximum width of around 500 nm, large enough that confinement effects can be ignored. A narrowing of the nanowires can be observed as we move towards its tip, where the width can be as low as a few tens of nanometers. This tapering effect is a consequence of the high growth temperatures that limit the diffusion of atoms from the sidewalls and the substrate surface to the top of the nanowire [23]. The measurement of the nanowires' length proves to be impossible from the SEM images alone. Figures 6.1a and 6.2a show however that their length is of the order of tens of micrometers.

Some of the gold nanorods used to functionalize both samples were deposited on a substrate in order to be observed. The images obtained (fig. 6.3a) puts their length between 60-80 nm and their width between 10-20 nm. Fig. 6.3b and 6.3c correspond to the functionalized nanowires, where numerous nanorods are clearly visible attached to the individual nanowires of sample BH1114-2 (fig. 6.3b and 6.3c) suggesting a successful functionalization. The images from the BH1115-2 sample didn't have the same level of detail, however deposits similar to those found on the BH1114-2 sample are also visible suggesting that the functionalization was equally successful.

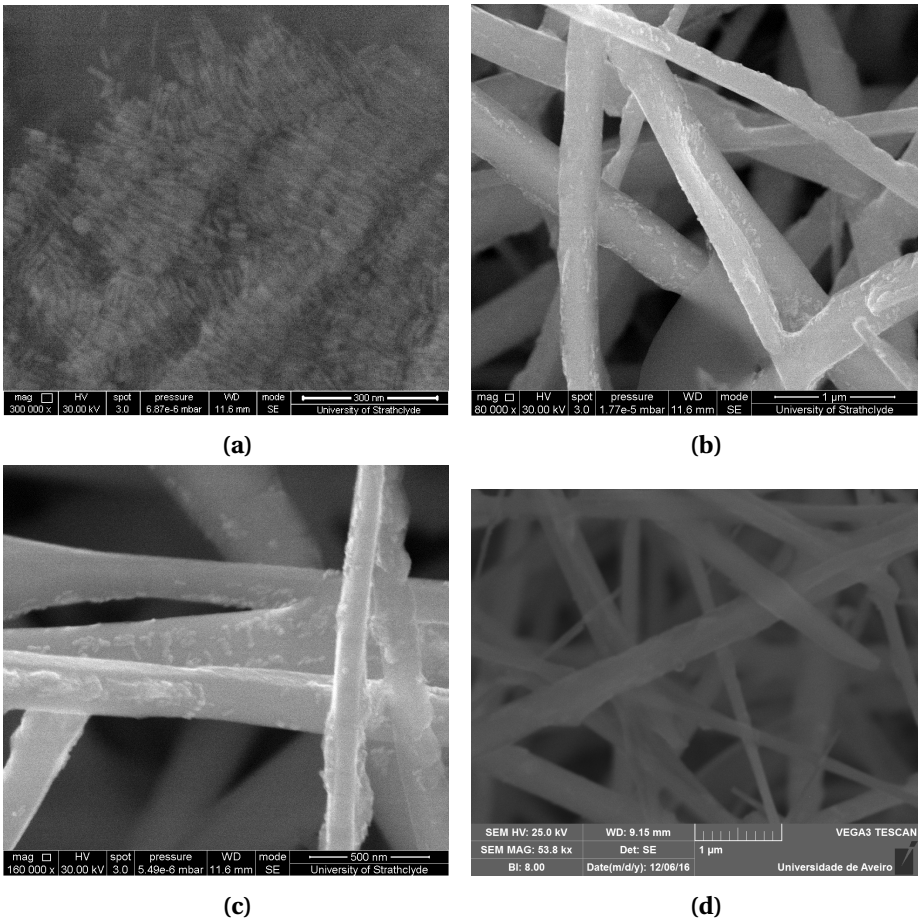


**Figure 6.3:** SEM topographical view from (a) the gold nanorods with which both samples were functionalized, (b-c) functionalized nanowires of sample BH1114-2 (d) and BH1115-2. The images show the nanorods attached to the nanowires' surfaces, specially those of sample BH1114-2 where a greater level of detail was possible.

## 6.2 Raman Spectroscopy

Further structural analysis was done via Raman spectroscopy in order to characterize the vibrational modes of the nanowires and identify their crystalline structures. All measurements were carried out on a Jobin Yvon HR800 spectrometer with backscattering configuration. The difraction grating was centred at 300 nm, the slit's width was 200 nm and a 100× magnifying lens was used. The sample remained at room temperature throughout the measurements and the excitation was carried out by the 632.8 nm line of a HeNe laser. Power density filters were used to avoid heating up the samples, damaging them in the process, and linear polarizers were placed after the excitation source and just before the detector so as to study the spectra dependence with the exciting light's polarization. The calibration of the equipment was performed by using a Si sample and monitoring its phonon mode at 520.0 $cm^{-1}$. Raman spectroscopy was performed on both samples, however due to the experimental results being identical we've chosen to present and discuss only those of the BH1115-2 sample.

When interpreting the results in this section we must take into consideration the different scattering facets of the nanowires, each with their own selection rules, and the geometry of the experiment which sees the nanowires seldom perpendicular to the incident beam, but instead slightly

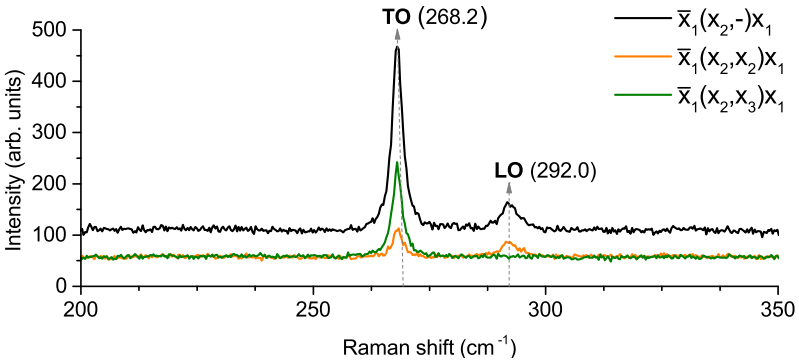


**Figure 6.4:** Raman spectra for the GaAs wetting layer from BH1115-2 for different polarization configurations.

tilted making a small angle with the substrate surface. For these two reasons the polarization dependencies often don't follow the selection rules strictly and modes which should be forbidden under certain polarization configurations will simply suffer a decrease in intensity instead.

The growth of the nanowires on both samples required first the deposition of a GaAs wetting layer on the substrate on top of which the nanowires grew. This layer's crystal structure is ZB and its Raman spectrum (fig. 6.4) shows the two expected peaks associated with the TO and LO mode of the crystal at 267.7 cm$^{-1}$ and 292.4 cm$^{-1}$, respectively. This values are close to the ones obtained from literature which predicts them to take place at 268.6 cm$^{-1}$ and 291.9 cm$^{-1}$ at room temperature [104]. A clear difference in intensity is visible, with the TO mode being much more intense in respect to the LO mode. This suggests that the incident light is focusing mostly on $\{11\bar{2}\}$ scattering facets since their selection rules match our observations (only the TO mode should be visible). By focusing on additional spots of the wetting layer we found that this is not always the case though and sometimes no mode ever completely vanishes, a result easily explained if we assume the wetting layer to be polycrystalline and to have, as a consequence, different scattering facets throughout it.

An analysis of single nanowires followed in a quest to find individual contributions from both the ZB and WZ phases and confirm the nanowires polytypic nature. Figure 6.5 shows the spectra

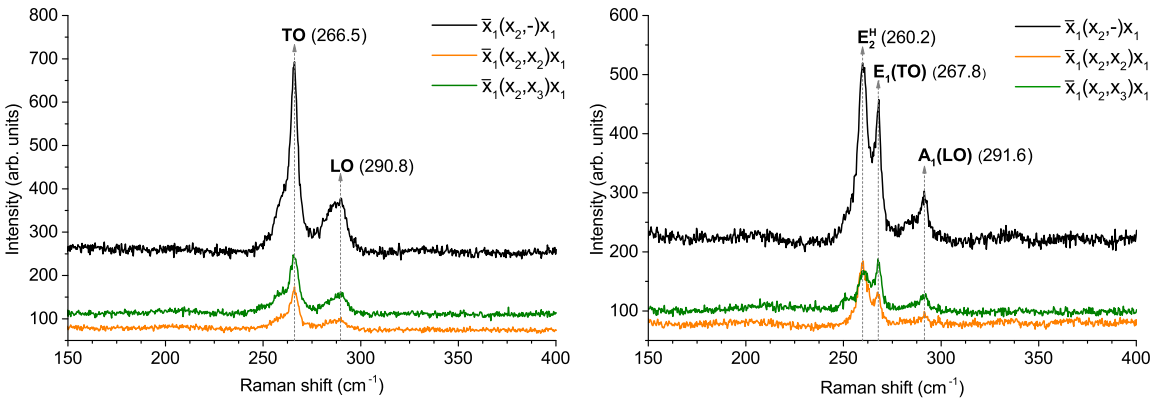


**Figure 6.5:** Raman spectra obtained for two different individual nanowires of the BH1115-2 sample, under different polarization configurations.

| | $E_2^H$ | $TO/E_1(TO)$ | $LO/A_1(LO)$ |
|---|---|---|---|
| fig. 6.4 | - | 268.2 | 292.0 |
| fig. 6.5a | - | 266.5 | 290.8 |
| fig. 6.5b | 260.2 | 267.8 | 291.6 |

**Table 6.1:** Active vibrational modes observed in the ZB GaAs wetting layer (fig. 6.4), and a ZB (fig. 6.5b) and WZ (Fig. 6.5b) region of two different GaAs nanowires from the BH1115-2 sample.

taken at two different nanowires with different polarization configurations. In the first spectrum (fig. 6.5a) we can observe two main peaks regardless of the polarization configuration, one at 266.5 $cm^{-1}$ and the other at 290.8 $cm^{-1}$. These, as mentioned before, are the peaks characteristic of ZB GaAs (TO and LO mode, respectively). However, despite the very low intensity it is possible to identify a shoulder in the lower frequency side of the TO band whose energy is close to that of the $E_2^H$ mode of WZ GaAs, which seems to indicate that although the region of analysis is mostly ZB, a slight contribution of WZ GaAs may exist.

The second spectrum (fig. 6.5b) shows three distinct peaks for all polarization configurations used: the first at 260.2 $cm^{-1}$, the second at 267.8 $cm^{-1}$ and the third at 291.6 $cm^{-1}$, which we will attribute to the $E_2^H$, $E_1$ (TO) and $A_1$ (LO) phonon modes characteristic of WZ GaAs, respectively. Nevertheless, we cannot discard the possibility of ZB contributions being present since the LO and TO modes of ZB GaAs have energies very close to the $E_1$ (TO) and $A_1$ (LO) modes of WZ GaAs. The $E_2^L$ mode, which should also be visible in our polarization configuration, is unfortunately outside of our measurement range and therefore can not be observed. As far as we know neither the $A_1$ (TO) nor the $E_1$ (LO) mode have been experimentally observed at this time [12, 86].

The Raman spectroscopy measurements were done under different polarization configurations, all of which are displayed in fig. 6.5. For the Raman spectrum of the GaAs ZB phase previously discussed (fig. 6.5a) we observe a significant decrease in the intensity of the TO mode for both the $\bar{x_1}(x_2,x_2)x_1$ and $\bar{x_1}(x_2,x_3)x_1$ configurations, however neither completely vanishes. As for the spectrum of GaAs WZ phase (fig. 6.5b), in the $\bar{x_1}(x_2,x_2)x_1$ configuration the $E_2^H$ mode's peak is the most intense although small contributions exist from the $E_1$ (TO) and $A_1$ (LO) modes (according to the selection rules only the $E_2^H$ mode should be visible), whereas for the $\bar{x_1}(x_2,x_3)x_1$ configuration the $E_2^H$ (TO) mode becomes less intense than the $E_1$ (TO) mode (selection rules only allow the $E_1$ (TO) and $A_1$ (LO) modes in this configuration).

It is not only our goal to find nanowires with different crystalline phases, but also to find evidence that these phases alternate along the axes of single nanowires. To do so individual nanowires in both samples were scanned along their axis until polytypism was observed. Fig. 6.6 shows the result of this procedure, with three different spectra taken at different spots in the same nanowire.

For the first and second spot two main peaks are seen at around the positions where the ZB GaAs TO and LO modes or WZ GaAs $E_1$ (TO) and $A_1$ (LO) modes are expected to be: 263.6 $cm^{-1}$/265.3 $cm^{-1}$ and 287.1 $cm^{-1}$/290.1 $cm^{-1}$ respectively. The observed lowering of the frequencies can be attributed to a different state of strain along the growth axis direction. The absence in spot 1 of any other distinct peaks confirms that we are focusing on a ZB GaAs rich zone. In spot 2, the emergence of a low intensity peak at 256.7 $cm^{-1}$ tells us that the spectrum has also a contribution of WZ phase, albeit small. The spectra of spot 3 is much more complex, presenting several overlapping Raman bands, some of them with a high width at half height. This shows that the structure in this region has suffered some damage, which could already exist or be a consequence of the incidence of the laser, whose power could be too high for the structural and thickness characteristics of the wire in this region.

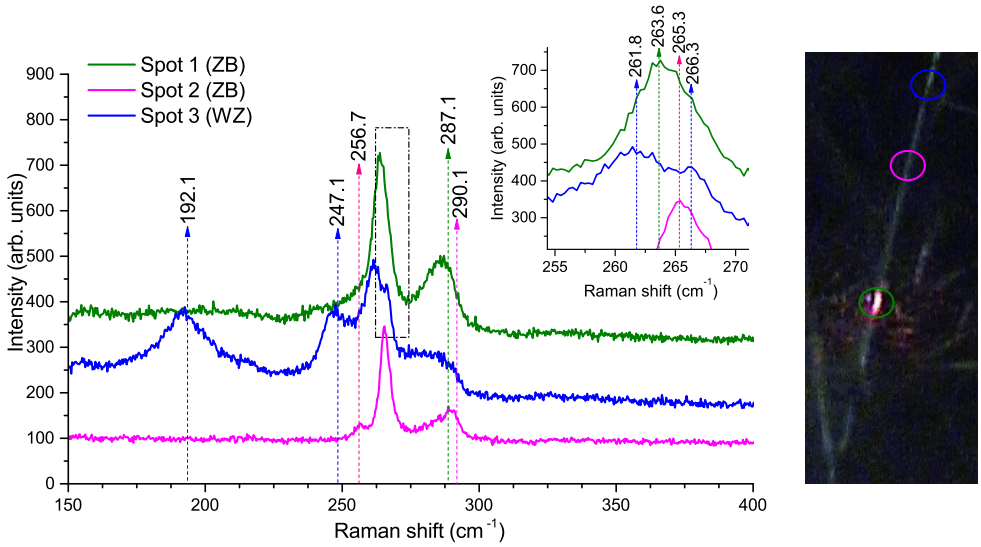


**Figure 6.6:** Raman spectra for three different spots in an individual NW from the BH1115-2 sample, a picture of which, obtained through an optical microscope, can be seen on the right with the spots identified. The different spectra show the presence of different phases along the nanowire.

| | $E_2^H$ | $TO/E_1(TO)$ | $LO/A_1(LO)$ |
|---|---|---|---|
| Spot 1 | - | 263.6 | 287.1 |
| Spot 2 | 256.7 | 265.3 | 290.1 |
| Spot 3 | 261.8 | 266.3 | 287.0 |

**Table 6.2:** Active vibrational modes from fig. 6.6.

Three of the observed peaks can be identified as phonon modes of ZB and WZ GaAs: the peaks at 266.3 cm$^{-1}$ and 287.1 cm$^{-1}$, as seen previously, can be attributed to the TO and LO modes of ZB GaAs and the $E_1$ (TO) and $A_1$ (LO) modes of WZ GaAs, while the peak at 261.8 cm$^{-1}$ can be attributed to the $E_2^H$ mode of WZ GaAs. It is also found that the band near the LO and $A_1$ (LO) frequencies is broader and at lower frequencies than we expected. The two remaining unidentified peaks at 192.1 cm$^{-1}$ and 247.1 cm$^{-1}$ must be explained, as neither can be attributed to GaAs. It is found that they are a consequence of the nanowires' oxidation due to the laser beam heating them up, causing permanent irreversible structural changes which will translate into additional vibrational modes [105, 106]. The relevant oxidation reactions for GaAs are [107]:

$$3O_2 + 2GaAs \rightarrow As_2O_3 + Ga_2O_3 \quad (1)$$
$$As_2O_3 + 2GaAs \rightarrow Ga_2O_3 + 4As \quad (2)$$

$$4O_2 + 2GaAs \rightarrow As_2O_5 + Ga_2O_3 \quad (3)$$
$$3As_2O_5 + 10GaAs \rightarrow 5Ga_2O_3 + 16As \quad (4)$$

The formation of both crystalline (c-As) and amorphous (a-As) arsenide as well as different oxides at the surface of our nanowires will "polute" it with contributions foreign to the vibrational modes of the nanowires. The longer the sample's laser exposure time the more oxides will be formed as can be seen in figure 6.7a, with some reactions being favoured over others depend-

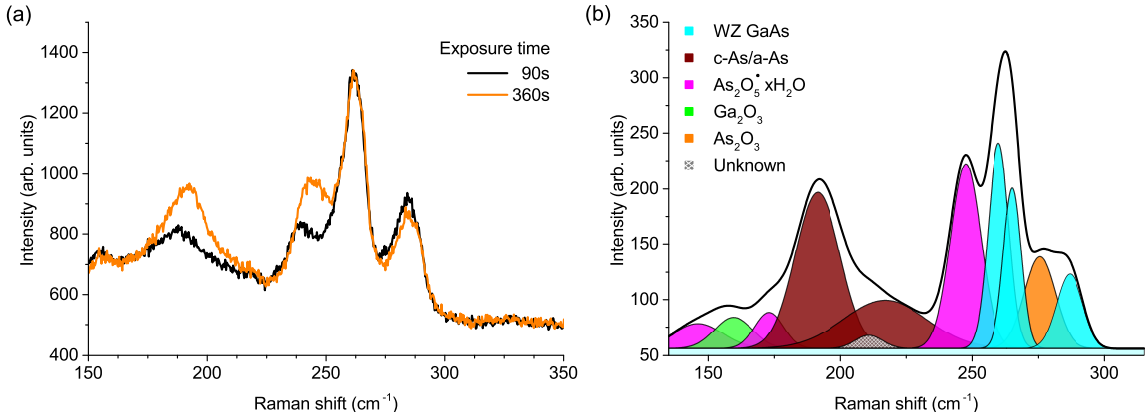


**Figure 6.7:** (a) Evidence of the oxidation of a nanowire after prolonged exposure to a laser (90 and 360s) and (b) deconvolution of the Raman spectrum of a WZ GaAs NW after exposure to laser light for 360 s.

ing on different factors, e.g. reaction (2) will be favoured in weak oxidation conditions, while the opposite occurs for reaction (3) [107]. By deconvoluting the WZ GaAs Raman spectrum using the oxides' known vibrational modes (table 6.3) we can identify the different contributions from the oxides (fig. 6.7b). Additionally, we find that the broad peak at around 220 cm$^{-1}$ and the sharper one at 190 cm$^{-1}$ can be attributed to the $E_g(TO)$ and $A_{1g}(LO)$ phonon modes of c-As. Mismatches between the expected and observed modes' energy are explained by the downshift in energy with the increase of temperature since our measurements were all done at room temperature whereas the vibration modes' values shown in table 6.3 were measured at 25 K [14, 108].

| $As_2O_3$ | $Ga_2O_3$ | $As_2O_3 \cdot xH_2O$ |
|---|---|---|
| 183.2 s | 170 w | 149.4 m |
| 268.1 s | 201.3 m | 179.5 m |
| | 260.3 w | 203.0 m |
| | | 246.5 s |
| | | 273.0 w |

**Table 6.3:** Vibrational modes of interest of the oxides formed in GaAs as a result of laser heating. The values, found in [14], are valid for a temperature of 25 K and don't take the light's polarization into account. The s, m and w labels stand for strong, medium and weak intensity.

Our results suggest that the different doping of both samples have no influence on their vibrational modes and ZB and WZ phases can be simultaneously found in both. An analysis of the vibrational modes after the functionalization with Au NPs was impossible due to the presence of gold nanorods and left over chemicals from the functionalization process.

## 6.3 Photoluminescence

Photoluminescence experiments were carried out at the University of Strathclyde for both samples before they were functionalized. The 325 nm line of a HeCd laser was used as exciting light, whose power was kept at 37 mW. The sample was placed within a vacuum sealed cryostat which was cooled with a cryofridge allowing for temperatures as low as 25 K. A 3-axis motion controlled

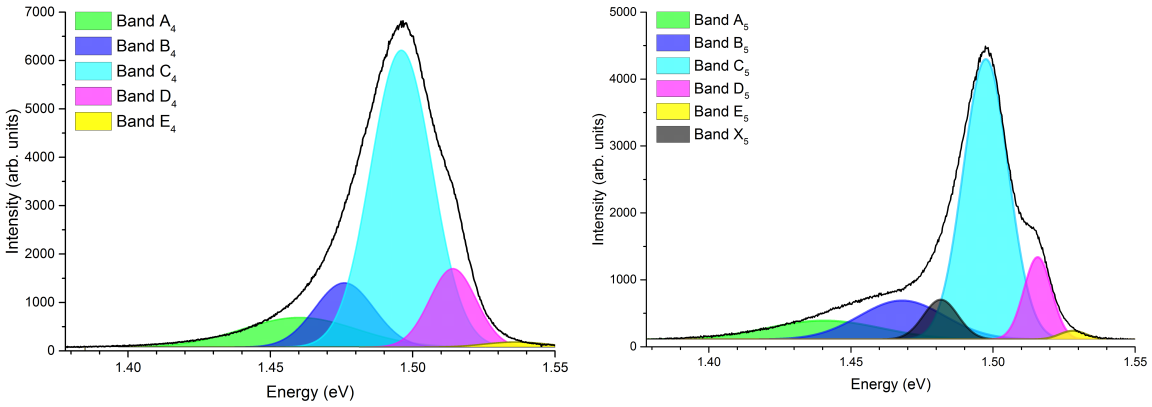


**Figure 6.8:** Photoluminescence from the BH1114-2 (left) and BH1115-2 sample (right) at 25 K and 30 K, respectively. The Gaussian components considered in the fit of each spectrum during its deconvolution are overlapped and labeled accordingly.

stage was used to modify the relative position of the cryostat in respect to the laser beam. An Oriel MS125 spectrometer with a MS125 77411 diffraction grating (1200 lines/mm, 360 nm blaze, 200-1000 nm range) and a slit width of 25 $\mu$m was used, while the luminescence was registered by a cooled Andor CCD detector.

The photoluminescence of both samples was obtained in identical conditions and within the same range of temperatures: from 25 K up to 160 K, at which point the signal was too weak for any useful information to be retrieved from it. The laser was focused on one of the nanowire regions available in each sample within which a large number of nanowires could be found. The spectra for both samples at low temperatures are shown in fig. 6.8. The shape of the luminescence for the two samples are somewhat similar: in both cases it is asymmetric due to the superposition of different individual emissions, both have their peak at around 1.496 eV and both have a shoulder on the high energy side at around 1.515 eV. A significant difference can be seen on the low energy side between the two spectra though: for BH1114-2 we have an exponential tail while for BH1115-2 we have a broad shoulder instead. It is seen however that for high enough temperatures (>50 K) this shoulder disappears being replaced by an exponential tail not unlike that seen in the BH1114-2 sample. These exponential band tails on the low energy side of the spectra are characteristic of recombinations involving localized carriers that are distributed along a band-tail state of the density of states [109, 110].

To characterize the optical properties of the nanowires, their luminescence as a function of temperature and excitation power was investigated. Our goal was to achieve a physical model capable of accurately describing and explaining the radiative transitions observed.

Based on the PL data acquired from the experiments, a model was developed for each sample on the basis that every individual emission takes the shape of a Gaussian curve and that the PL spectra, in the two types of dependencies mentioned before, were fitted with the minimum number of bands possible capable of providing an adequate fit. A five band model was initially considered for both samples, with each band named $A_i$ to $E_i$, where the $i = 4,5$ stands for the respective sample. While this model proved to be adequate for the BH1114-2 sample, the extra low energy shoulder in the BH1115-2 sample required us to add an extra band we named $X_5$. The just mentioned components of each model are shown in fig. 6.8, overlapped to the PL signal taken at a temperature of 25 K and 30 K, where the components of the BH1115-2 sample can be seen to be noticeably sharper than those of the BH1114-2 sample. The colours and labels assigned to each component will stay the same throughout the remainder of our discussion.

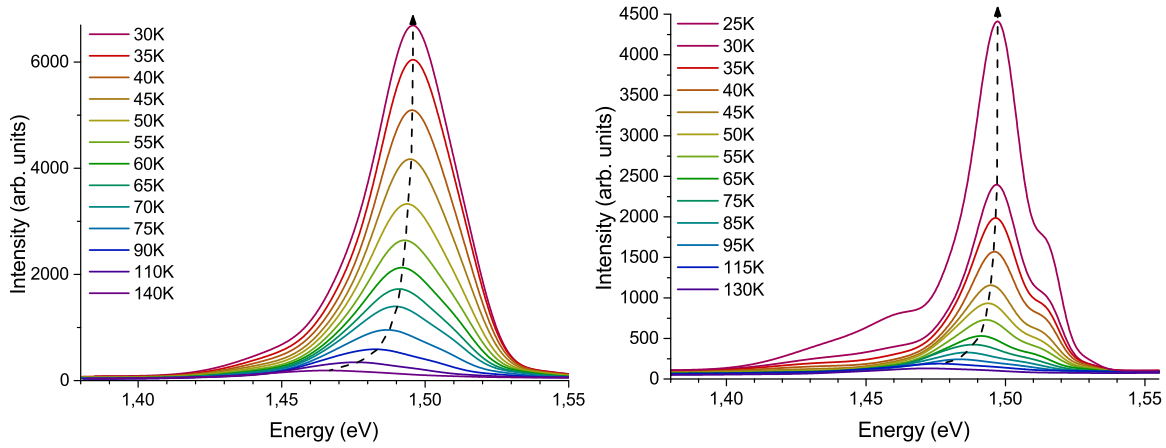


**Figure 6.9:** PL spectra of the BH1114-2 (left) and BH1115-2 (right) samples for temperatures between 30 K and 150 K.

### 6.3.1 Temperature dependent photoluminescence

To understand the radiative mechanisms involved in the measured PL we must study the dependence on the temperature of each one of the Gaussian components in the fitting model. The most intense spectrum, i.e. the one taken at the lowest temperature, was deconvoluted first and from there we moved on to the remaining spectra in increasing order of temperature. The deconvolution of any given spectrum was always based on the previous spectrum's calculated fitting parameters.

A first look at our experimental results (fig. 6.9) shows that the increase of temperature is accompanied by a decrease in PL intensity and a shift towards lower energies of the emission peak, a behaviour typical of semiconductors. It is also noticeable that the lower energy side shoulder of sample BH1115-2 decays considerably quicker than the rest of the band, being barely visible for temperatures greater than 50 K.

The results displayed in figure 6.10 were obtained by applying our proposed fit methodology for all the PL spectra measured during the temperature dependent experiment. The temperature dependency of the peak position of each component was further fitted with the previously discussed Pässler equation (eq. 5.6) so as to give us an idea of how the behaviour of each component (table 6.4) compares with the extensively studied behaviour of the bandgap of ZB GaAs bandgap energy.

The BH1114-2 sample has an energy temperature dependence typical of semiconductors with all its components showing a monotonic energetic redshift that was easily fitted. For temperatures T<100 K we find different behaviours from the different components, with $C_4$, $D_4$ and to a lesser extent $B_4$ having similar dependencies with temperature. As for temperatures beyond 100 K, all components seem to approximately follow the ZB GaAs bandgap temperature dependence, a trend which is reflected by the similar values of $\alpha$, the parameter that defines the limiting slope of the energy curve for high temperatures. In fact the $\alpha$ of ZB GaAs lies within the error interval of all the components of the BH1114-2 sample except for $B_4$.

Of all the components, the $C_4$ is the one that follows the ZB energy curve the best as reflected by the similar fitting parameters. Another important feature of our results is the fact that the $E_4$ component's energy lays above the ZB bandgap. In fact, the same is observed for the $E_5$ band that will be discussed shortly. We hypothesize that this component is either the result of transitions across the WZ GaAs bandgap, whose energy is unknown at this point, or the result of intraband transitions across the ZB or WZ bandgap that take place at higher energies than expected as a

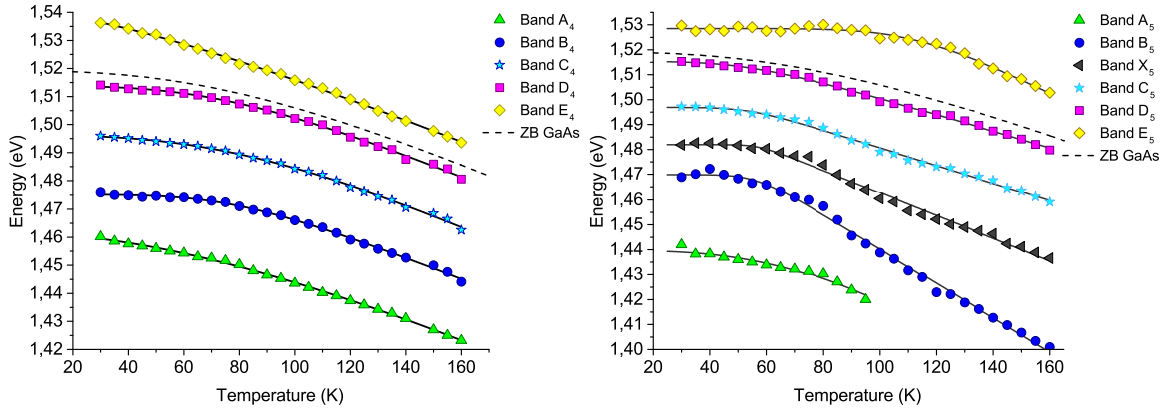


**Figure 6.10:** Temperature dependence of the components under our model for BH1114-2 (left) and BH1115-2 (right) samples. The energy error varied from ~$10^{-5}$ at 25 K to ~$10^{-4}$ at 160 K. The Pässler's fitting equation (eq. 5.6) can be found overlapped on the experimental results.

result of confinement effects.

The energy curves of the BH1115-2 sample's components showed to have a slightly more atypical behaviour than those of the BH1114-2 sample. The $A_5$ component experiences a redshift with increasing temperature, however its intensity decreases quickly and at 95 K the component ceases to exist. The $B_5$ component experiences a similar redshift but as it approaches higher temperatures it shows to redshift at a faster rate than the remaining components. The $E_5$ component also lays above the ZB GaAs bandgap not unlike its homologous for sample BH1114-2. However, it has the added feature of not experiencing any shift until temperatures of around 90 K, something unique to this component. Attention must be given to the large errors obtained for some of the parameters of the $A_{4/5}$ and $E_{4/5}$ components, specially for the average phonon temperature. This seemed to be the trend throughout much of our work as a result of fitting complication to both bands because of their low intensity or large width. For this reason the discussion throughout the remainder of this section may not include these components.

| | Component | E(T=0 K) (eV) | $\alpha$ (meVK$^{-1}$) | $\Theta$ (K) | p |
|---|---|---|---|---|---|
| **BH1114-2** | **$A_4$** | 1.46154 ± 0.00082 | 0.52 ± 0.16 | 321 ± 265 | 1.83 ± 0.28 |
| | **$B_4$** | 1.47525 ± 0.00025 | 0.388 ± 0.021 | 167.7 ± 8.8 | 4.94 ± 0.67 |
| | **$C_4$** | 1.49617 ± 0.00045 | 0.477 ± 0.074 | 216 ± 48 | 2.85 ± 0.41 |
| | **$D_4$** | 1.51377 ± 0.00043 | 0.429 ± 0.045 | 182 ± 25 | 3.35 ± 0.52 |
| | **$E_4$** | 1.5406 ± 0.0017 | 0.440 ± 0.082 | 195 ± 213 | 1.56 ± 0.40 |
| **BH1115-2** | **$A_5$** | 1.4398 ± 0.0014 | 0.8 ± 1.9 | 198 ± 389 | 3.1 ± 2.2 |
| | **$B_5$** | 1.47002 ± 0.00080 | 0.688 ± 0.016 | 113.3 ± 3.6 | 10.7 ± 5.3 |
| | **$X_5$** | 1.48202 ± 0.00061 | 0.45 ± 0.012 | 114.4 ± 4.1 | 18 ± 20 |
| | **$C_5$** | 1.49703 ± 0.00044 | 0.3558 ± 0.0088 | 108.5 ± 3.7 | 8.1 ± 3.0 |
| | **$D_5$** | 1.51537 ± 0.00048 | 0.341 ± 0.015 | 117.1 ± 7.3 | 4.4 ± 1.0 |
| | **$E_5$** | 1.52853 ± 0.00030 | 0.573 ± 0.099 | 231 ± 17 | 8.5 ± 2.1 |
| **Bulk GaAs (Ref. [95])** | | 1.51909 | 0.4730 | 225.6 | 2.513 |

**Table 6.4:** Fitting parameters from eq. 5.6 as calculated for all of both samples' components. The known fitting parameters for ZB GaAs are also included for the sake of comparison.

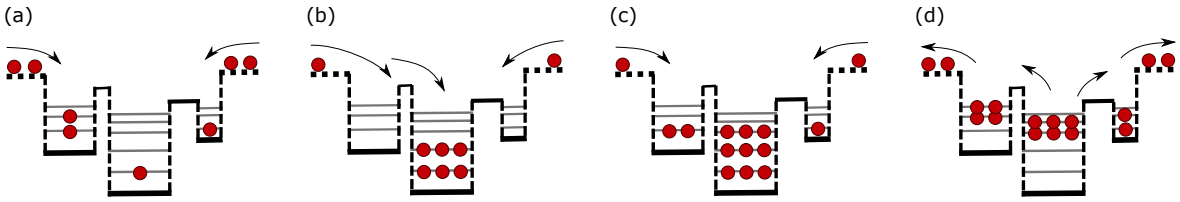


**Figure 6.11:** Illustration of the four phases of the anomalous S-shaped behaviour in the conduction bands of polytypic GaAs. The black arrows represent the thermal escape of carriers over potential barriers. A description of this phenomenon can be found in the discussion of the temperature dependent PL results.

The $X_5$, $C_5$ and $D_5$ components are the ones that resemble the ZB GaAs bandgap behaviour the most, however this isn't reflected by the respective calculated fitting parameters from the Pässler equation. A more careful look at these components' energy curves shows us why: instead of a smooth monotonic decrease of energy with increasing temperature what we observe instead is what can be described as a redshift of the components at different rates over different temperature intervals: for T<80 K all components show a normal energetic redshift, however from 80 K to 120 K the rate at which the components' energies decrease slows down, before pacing back up again and returning to a normal behaviour from 120 K onwards. We have no reason to believe there was any kind of laser power or temperature fluctuations during our experiment that could justify these observations.

Most likely, the described behaviour is the result of simple experimental errors or less than perfect fits, however we must investigate the possibility of it having physical significance. If we assume our samples' nanowires to have a good degree of potential fluctuations along their axes, as a consequence of WZ/ZB segments of different widths, we can raise the hypothesis that what we are observing is a tamer manifestation of the commonly called "S-shaped behaviour" [111, 112] observed in many materials who also have potential fluctuations such as GaN and (Ga,In,N,As)/(Ga,As,N) multiple quantum wells [113] and polytypic GaAs nanowires [114]. This phenomenon is characterized by a red-blue-redshift of the energy and for polytypic GaAs nanowires it can be explained as follows: the sequence of alternating ZB and WZ sections of different widths along the nanowires' axes causes a fluctuating potential with multiple local minima as illustrated in fig. 6.11. For very low temperatures the carriers won't have enough thermal energy to overcome the potential barriers and will be randomly trapped in these local potential minima (fig. 6.11a). As the temperature increases from very low temperatures up to T≈80 K weakly localized carriers acquire enough thermal energy to overcome the potential barriers that keep them trapped and relax down to absolute potential minima via hopping resulting in the observed redshift in energy (fig. 6.11b) [115]. As we increase the temperature from T≈80 K up to T≈120 K the carriers acquire enough thermal energy to fill higher-energy localized states from the band tail (fig. 6.11c) leading to the energetic blueshift. Finally, for temperatures beyond T≈120 K the carriers' thermal energy doesn't allow for the localization of the carriers and the recombinations take place instead between delocalized states (fig. 6.11d) leading to the final observed redshift typical of a regular thermalization of carriers.

The strength of this anomalous behaviour will depend on the exciting light's power (the lower it is the stronger the localization effect) and on the degree of potential fluctuation present in the material [114]. The forthcoming discussion in this section will not only continue investigating the physical properties of our samples but also determine whether or not the slightly anomalous energy dependency of the BH1115-2 sample is indeed a consequence of this effect.

The evolution of the full width at half maximum (FWHM) of each component (fig. 6.12) gives

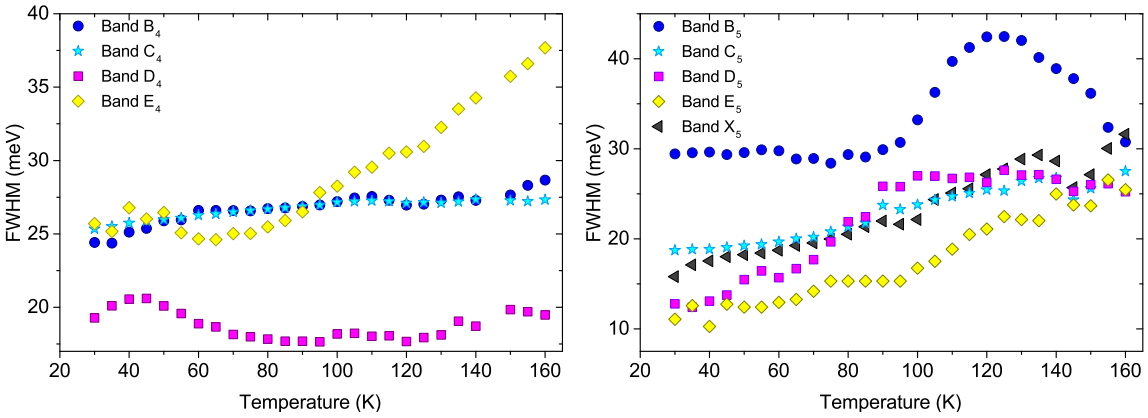


**Figure 6.12:** Full width at half maximum of each component considered in the models for the BH1114-2 (left) and BH1115-2 (right) sample. A general increase with temperature can be seen in both, specially that of the BH1115-2 sample.

us additional information about the observed transitions. For the BH1114-2 sample, with the increase of temperature, the FWHM of the $E_4$ component increases significantly, whereas in the case of $B_4$ and $C_4$ a small increase is observed, and for $D_4$ the FWHM stays mostly constant. On the other hand all the BH1115-2 sample's components, with the exception of $B_5$, experience a considerable increase in FWHM with increasing temperature. This goes in accordance to what was expected: an almost constant dependence on temperature for low temperatures followed by a monotonic increase resulting from the thermal broadening of the emissions [112, 116].

#### 6.3.1.1 PL intensity quenching

As was previously discussed the PL intensity quenching gives us insight into the non-radiative recombination channels present in the sample. Based on the model proposed earlier, the thermal extinction of the different radiative transitions can be described by equation 5.7 which takes into consideration the thermal activation of two different quenching channels: one involving discrete energy levels and the other involving the promotion of carriers trapped in quantum wells to the adjacent conduction band. To fit our experimental data we considered different contributions from these two quenching channels and looked for the model that made the most physical sense while using the minimum number of de-excitation channels. The parameters $c_i$, which as seen earlier are proportional to the ratio between the degenerescence of the higher energy level and of the radiative state, also serves as an indication of whether a non-radiative band state should be considered instead or in addition to excited/defect non-radiative states since a large value of $c_i$ indicates that the excited/defect state corresponds to a band state. For our data we considered a maximum of two excited states and a band state.

The thermal quenching of each component can be seen in fig. 6.13 as a function of the reciprocal temperature in an Arrhenius plot. The activation energies extracted from the experimental data can be found in table 6.5.

We found that the same model was used across the two samples for equivalent components. For the lower energy components, $B_4$, $B_5$, $C_4$ and $C_5$, the best fitting model included quenching channels related to two discrete excited levels. Despite the common model used for these components, we notice that the energies of the discrete excited levels of the BH1115-2 sample are greater than those of BH1114-2, with the exception of the first excited state of $C_5$. The calculated energies also show that for the $C_4$ and $C_5$ components the second excited state lays above the bandgap of ZB

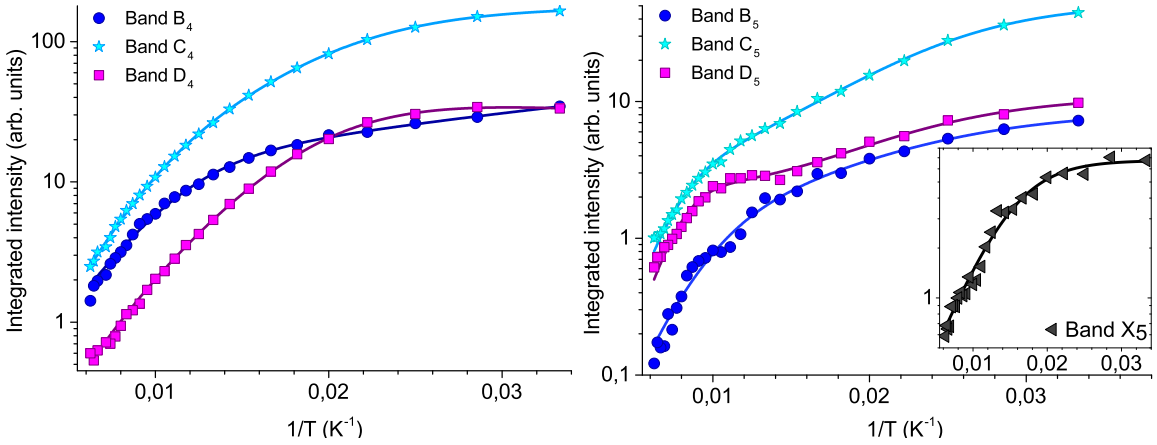


**Figure 6.13:** Integrated intensity for each component considered in our models as a function of temperature plotted in an Arrhenius plot for the sample BH1114-2 (left) and BH1115-2 (right). The data of the $X_5$ component is displayed in a subplot for visualization purposes.

GaAs.

For the $D_4$ and $D_5$ components the model was based on the coexistence of two non-radiative de-excitation channels: one involving a single discrete excited state and the other a band. Not unlike the already discussed components, the energies of $E_1$ and $E_b$ for $D_4$ and $D_5$ are also greater for sample BH1115-2 than on BH1114-2. Furthermore, the energy $E_b$ puts the energy of the conduction band above the ZB GaAs bandgap by a considerable amount in both sample, specially BH1115-2.

For the $X_5$ band the model we used consisted on a single quenching channel involving a band. In this case, the channel's activation energy lays slightly below the ZB GaAs bandgap.

As was just discussed, many of the quenching channels considered included discrete energy levels ($E_2$) or ionization energy levels ($E_b$) above the bandgap of ZB GaAs. This can be explained if we assume our nanowires to comprise very thin segments of ZB GaAs that due to confinement effects will see their conduction band energies raised. Under such a model high energies of $E_b$ can be explained since the energy required of a trapped electron to escape a quantum well is now much higher and, following this same reasoning, the non-radiative excited states found in the ZB

| | Component | E(T = 0K) (eV) | $E_1$ (meV) | $E_2$ (meV) | $E_b$ (meV) |
|---|---|---|---|---|---|
| **BH1114-2** | $B_4$ | 1.47525 ± 0.00025 | 3.4 ± 1.7 | 33.6 ± 2.0 | ——— |
| | $X_4$ | ——— | ——— | ——— | ——— |
| | $C_4$ | 1.49617 ± 0.00045 | 18.53 ± 0.26 | 49.4 ± 2.3 | ——— |
| | $D_4$ | 1.51377 ± 0.00043 | 3.0 ± 1.5 | ——— | 15.82 ± 0.81 |
| **BH1115-2** | $B_5$ | 1.47002 ± 0.00080 | 12.1 ± 1.6 | 48.8 ± 9.3 | ——— |
| | $X_5$ | 1.48202 ± 0.00061 | ——— | ——— | 10.5 ± 1.3 |
| | $C_5$ | 1.49703 ± 0.00044 | 15.17 ± 0.34 | 89 ± 26 | ——— |
| | $D_5$ | 1.51537 ± 0.00048 | 9.22 ± 0.92 | ——— | 78 ± 29 |

**Table 6.5:** Activation energies obtained by fitting the experimental data from the intensity quenching with function 5.7. The components' energies at 0 K obtained earlier from Pässler equation are also shown.

segments can now also be found at higher energies.

### 6.3.2 Power dependent photoluminescence

A study of the power dependence for both samples was performed at the University of Strathclyde with the same setup as the one used and already described for the temperature dependency. The sample was kept at a constant temperature of 25 K and the power, originally 37 mW, was reduced by placing neutral density filters on the incident laser beam's optical path. Measurements were performed over a range of over one order of magnitude down to values as low as 3% of the laser's original power.

The deconvolution of the measured spectra was performed taking into account the previously proposed model of Gaussian components. As the excitation power was increased the intensities of the different components increased too, but at different rates. A log(I)-log(P) plot (fig. 6.14) was drawn to study this dependence and a linear fit was performed on the experimental measurements of each component yielding the results shown in table 6.6.

| | **parameter** $m$ | | |
|---|---|---|---|
| **component** | **C** | **D** | **X** |
| **BH1114-2** | 0.881 ± 0.063 | 0.871 ± 0.063 | – |
| **BH1115-2** | 0.94 ± 0.11 | 0.995 ± 0.064 | 1.074 ± 0.066 |

**Table 6.6:** Parameter $m$ as described in eq. 5.8 for the adjusted Gaussian components of each sample.

The fitting of both samples' PL power dependency for the $B_4$ and $B_5$ components was problematic due to the PL behaviour at powers below 10 mW, where the intensity of the lower energy emissions seems to suddenly decrease with increasing power (fig. 6.14), and the high sensibility those components showed to the behaviour of the two adjacent components, $A_{4/5}$ and $C_{4/5}$. This results in a high dispersion of the fitted parameters from the integrated PL vs power relationship that didn't allow us to reach a meaningful physical explanation capable of supporting such results.

Setting aside the $B_4/B_5$ components, all the remaining ones have a linear power dependency. The calculated parameter $m$ varies between the two samples: for BH1114-2 sample we have $m < 1$, whereas for the BH1115-2 sample we have $1 < m < 2$, with the exception of $C_5$. No conclusions could be done about this last component as its value of $m$ and the respective error interval can put it both below or above unity. We hypothesize however, based on the behaviour of the BH1115-2 sample's remaining components, that it too owes its emission to the recombinations of bound excitons.

The calculated values of $m$ for the $C_4$ and $D_4$ components are consistent with either free-to-bound or donor-to-acceptor recombinations. On the other hand, the determined parameter $m$ for components $D_5$ and $X_5$ from the BH1115-2 sample indicates that the emissions result from either free or bound excitons recombinations [100]. The higher doping concentration of this sample suggests that the latter case is the most likely, that is, the emissions come from bound exciton recombinations.

At this point we must refer back to the hypothesis we raised earlier regarding the presence of potential fluctuation in the BH1115-2 sample that, in turn, caused a soft S-shaped temperature dependence. The PL power dependency for this sample indicates that the transitions taking place are a result of the recombination of excitons, either free or bound to defects. This is however inconsistent with the presence of potential fluctuation in the material, as in such cases the formation of excitons can't take place [117]. Therefore the power dependent PL results seem to rule

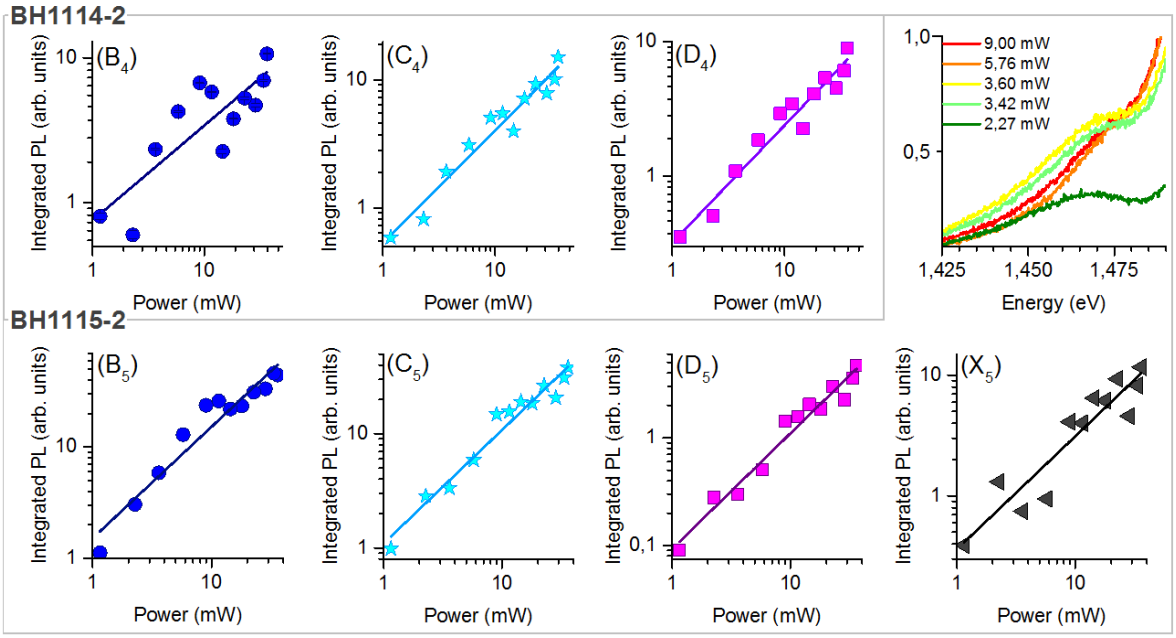


**Figure 6.14:** On the top right corner we find the PL spectra obtained for sample BH1115-2 under different powers of excitation light. The remaining pictures, accordingly labeled with the component they refer to ($B_4$-$D_5$), show the the linear dependence of the PL intensity with exciting power (max value of 37 mW) on a log-log plot for each component of each sample.

out the possibility of our samples having a degree of potential fluctuations big enough to warrant an S-shaped effect. Additional PL experiments at lower exciting powers can be done in the future to completely rule out this hypothesis since the strength of this effect increases with decreasing excitation power.

Power dependent PL can also be used to investigate whether or not the observed emissions are in fact spatially indirect. If the GaAs nanowires have indeed type II band alignment we can expect the photoexcited carriers to be spatially separated, with electrons confined in the ZB QWs and holes in the WZ QWs. As a result a Hartree electrostatic potential should appear across the ZB/WZ interface resulting in the bending of the valence and conduction bands of both phases (top left corner of fig. 6.15) [118]. This bending creates a triangular confinement region where the electrons will be trapped within different energy levels related to how narrow the region is. With increasing excitation power the confinement regions narrow which in turn leads to a larger energetic separation between the trapped electrons and holes. For that reason the energy of emissions taking place across the ZB/WZ interface will blueshift. It has been shown that for type II heterostructures this blueshift is proportional to the cube root of the excitation power [119, 120].

$$E \propto P^{1/3} \tag{6.1}$$

In materials with spatially direct transitions there isn't any band bending taking place since the carriers don't accumulate at the ends of the quantum wells and consequently emissions remain at the same energetic position regardless of the excition power.

The plots of the energetic shift with the third root of the exciting power for each component of each sample are displayed in fig. 6.15. Even taking into account the dispersion and experimental error, with the exception of $D_5$ all components show a blueshift of energy in accordance with our

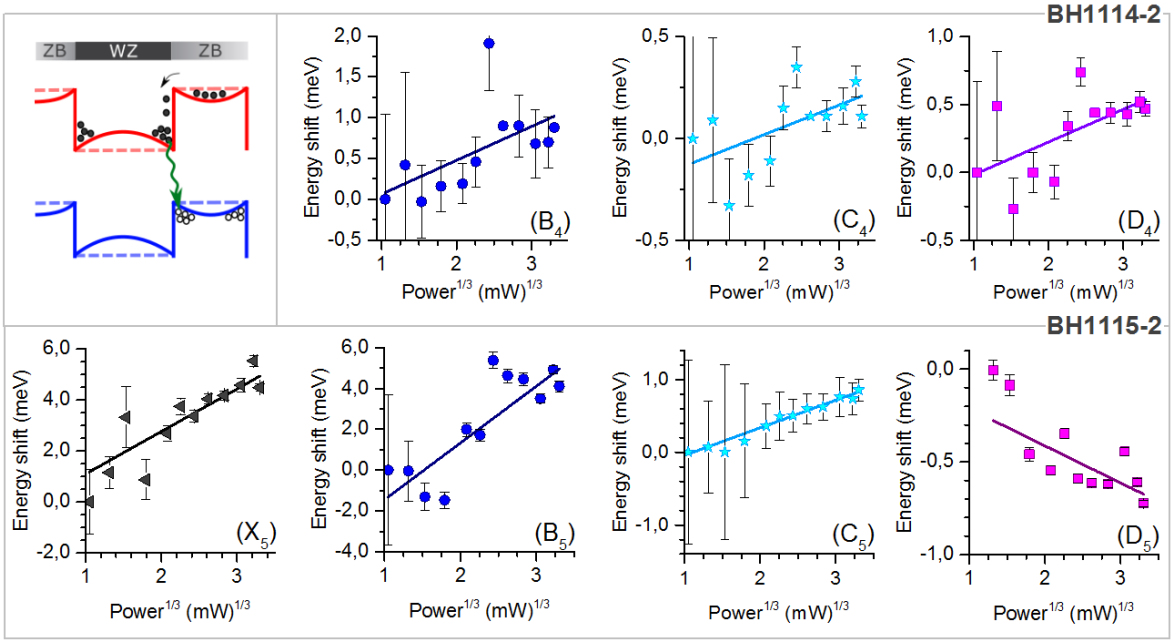


**Figure 6.15:** (a) Illustration of the band bending effect in polytypic GaAs nanowires (top left corner) and the plots, accordingly labeled, of the energetic shifts of the components of interest from the energy measured at the lowest excitation power.

assumption that they take place across the WZ/ZB or ZB/WZ interface. We are unsure whether the apparent energetic redshift that the $D_5$ component experiences is a result of a poor fit or an accurate description of the emission's behaviour. As of now we see no reason that would explain a shift towards lower energies with increasing power.

## 6.4 Photoluminescence Excitation

Photoluminescence excitation (PLE) was performed at the University of Strathclyde with the same setup as the one used for the previous photoluminescence experiments, but with a Xe lamp and a monochromator used to cover different excitation wavelengths. The sample was placed in a vacuum-sealed cryostat and remained at a temperature of 15 K throughout the whole experiment. Due to time constraints only the sample BH1114-2 before its functionalization was studied. Furthermore, limitations in the experimental setup only allowed us to perform PLE on the end tail of the emission's low energy side in the energy range of 1.4433 eV to 1.4595 eV. All the spectra obtained from this experiment can be found in fig. 6.16 alongside an illustration identifying the monitored energies.

For the highest detection energy measured in our work, 1.4595 eV, we have mainly emissions from the $A_4$ and $B_4$ components, assuming the fitting model to the PL spectra considered previously. The single absorption channel identified for this detection energy lays at 1.488 eV, and the lack of additional peaks means that the channel is the source of both the $A_4$ and $B_4$ luminescence, although we can't conclude that no other absorption channels would show up if we measured at higher detection energies.

As we shift the detection range to lower energies a new peak arises in the spectra shifted by around 18.3 meV towards lower energies. This new absorption channel will contribute to the luminescence of the $A_4$ component alone and suggests that this component comprises at least

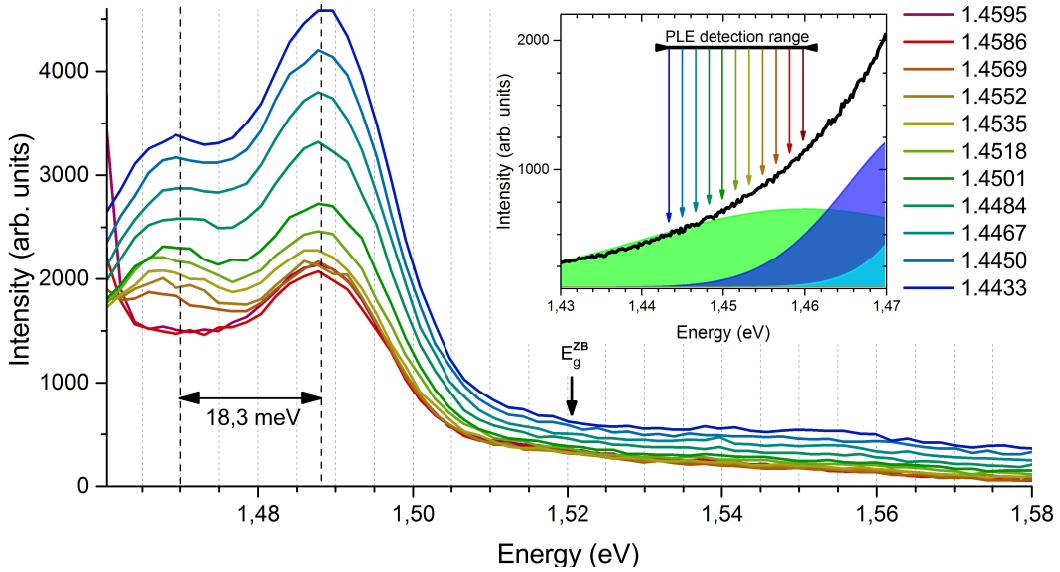


**Figure 6.16:** PLE spectrum for the BH1114-2 sample with two distinct peaks. The detection energies, which varied from 1.44336 eV to 1.45949 eV, are represented in the subplot by coloured arrows.

two individual emissions. The PLE results show that the tail emissions of the PL spectrum, below 1.4595 eV, result from the contributions of at least two absorption bands located below the ZB band gap, confirming thus the existence of electronic localized energy states.

The small detection range used doesn't allow us to extract more information out of the spectra or deepen our discussion. We leave as a suggestion for a future work to repeat PLE covering ideally the whole transition. Furthermore, relevant information about the material can be further retrieved by monitoring the PL in a resonant condition, i.e. with an excitation wavelength set to one of the peaks obtained from PLE, and by performing time dependent PL in order to identify and distinguish the emission channels' optical nature.

## 6.5 Cathodoluminescence

Cathodoluminescence was performed at the University of Strathclyde on both samples before they were functionalized. The spectra maps for a region of 10 µm × 10 µm and 5 µm × 5 µm is shown in fig. 6.17 for the BH1114-2 and BH1115-2 samples, respectively. A clear difference in intensity between different nanowires or even within a single nanowire is observed from the measurements. This is not due to intrinsic properties of the nanowires but instead because of their random orientation that covers different planes of depth making focusing on all nanowires or even on a full nanowire impossible.

The luminescence of both samples is relatively weak at room temperature but we can nonetheless clearly identify distinct emissions. The energies of the observed individual emissions was estimated by analysing the CL map and checking the CL spectra in different spots of the samples, although the low signal-to-noise ratio made this last task challenging. Based on this procedure we identified two main emissions for the BH1114-2, at around 1.38 eV and 1.40 eV, and three for the BH1115-2 sample, at around 1.38 eV, 1.41 eV and 1.43 eV. This last emission from sample BH1115-2, at 1.43 eV, shows to be present in zones of lower intensity in respect to the other two emissions observed in this sample. The spatial separation of different emissions along the growth axis of

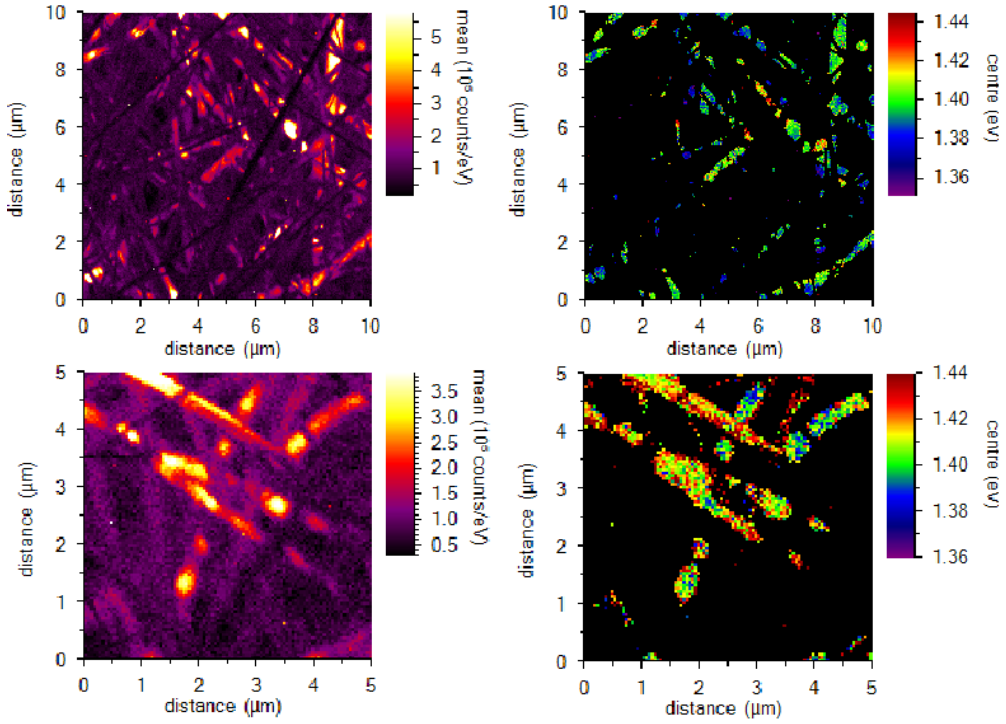


**Figure 6.17:** Mean intensity (left) and peak center position from the most luminescent areas (right) for the BH1114-2 (top) and BH1115-2 (bottom) samples. The peak center position is only displayed for the most intense regions of the spectra map.

NWs further supports the notion that our nanowires have polytypic nature.

Building on the temperature dependent PL discussed earlier the expected energy of each of our model's components was estimated at room temperature (293 K). Based on those we can extrapolate that the two observed CL emissions of the BH1114-2 sample (1.38 eV and 1.40 eV) come from the $B_4$ and $C_4$ components, which at room temperature take place at 1.384 eV and 1.409 eV, respectively, whereas the three observed for the BH1115-2 sample (1.38 eV, 1.41 eV and 1.43 eV) can be attributed to the $X_5$, $C_5$ and $D_5$ components, that take place at 1.375 eV, 1.412 eV and 1.435 eV, respectively.

## 6.6 Post-functionalization characterization

Several gold nanorods with different aspect ratios were synthesized at the University of Strathclyde through the seed-mediated growth method. The nanorods chosen to functionalize our samples were the ones that exhibited the best longitudinal-to-transverse mode intensity ratio, which can be seen in the absorbance spectrum of fig. 6.18, and lowest dispersion of sizes. The fact that both resonant modes are at energies higher than the samples' emissions (fig. 6.18) is important as it means that plasmonic enhancement of the nanowires' emissions can be ruled out and any observed PL change should be interpreted considering other effects, namely the electrostatic effects due to the presence of metal nanoparticles.

The functionalization of the BH1114-2 and BH1115-2 samples was performed at the University of Strathclyde and University of Aveiro, respectively. Careful attention was given to the procedure in order to ensure that both samples were functionalized identically. Even though both samples were fuctionalized in the same way logistical reasons made it so that a direct comparison under

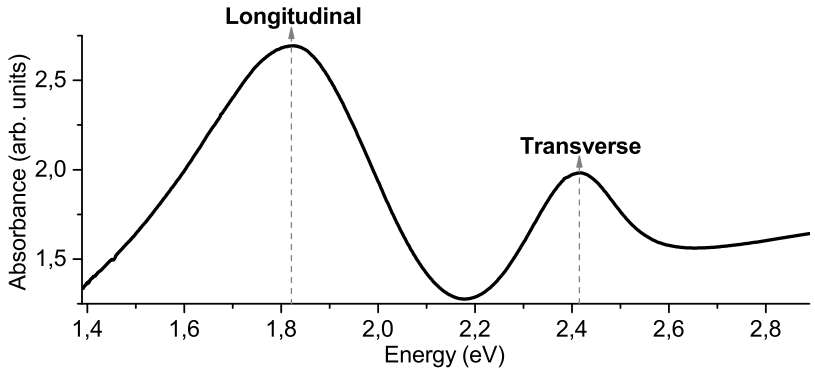


**Figure 6.18:** Absorbance spectrum of the nanorods used to functionalize both samples with the longitudinal and transverse resonant modes labeled.

the same experimental setup was only possible for sample BH1115-2.

PL experiments were done again on the BH1115-2 sample but this time at the University of Aveiro with a different experimental setup. The excitation was performed by the 514.5 nm laser line of an $Ar^+$ laser with an exciting power of 80 mW. Only liquid nitrogen was available and therefore the lowest temperature we could perform measurements at was 70 K. The results before and after the functionalization are displayed on fig. 6.19a.

Handling the experimental results proved to be difficult due to the spectra's low signal-to-noise ratio. Nonetheless some distinctions between the two spectra are noticeable: the spectrum measured post-functionalization seems to be blueshifted ever so slightly and its shape on the high energy side seems to be more intense leading to a more symmetrical emission. In an attempt to get a clearer view of the emissions before and after functionalization we fitted both with a superposition of multiple Gaussian curves with no consideration for their actual physical significance - the goal was merely to filter the noise that kept us from interpreting the results (fig. 6.19b). The resulting fitted spectra confirmed that there was indeed a small energetic shift of the emissions' peaks towards higher energies after the sample was functionalized. This shift was calculated to be ~4 meV.

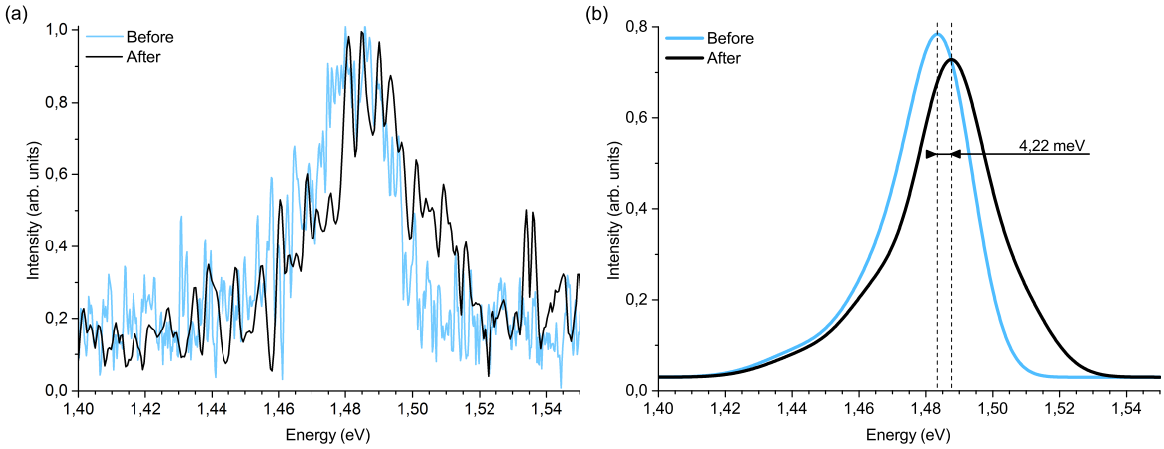


**Figure 6.19:** Normalized PL spectra of the BH1115-2 sample at 70 K and 30 mW exciting power before and after the nanowires' functionalization (left) and a fit done to the PL spectra in a quest to resolve the emission.

The change in shape of the luminescence can be attributed to the inhomogeneous distribution of nanorods on the sample. Only a finite number of nanorods are present in the sample, and naturally their concentration varies from place to place. It is then not surprising that in some of those places the lack of nearby nanorods leads to no shift in energy, and therefore the emission takes place with the same energy as before functionalization. For this reason the spectrum won't shift as a whole but instead it will broaden as a result of the superposition of shifted and non-shifted emissions from the nanowires.

The blueshift observed in the PL peak can be explained by the ICE. A small gold NP in the surface of a GaAs nanowire will act as a point charge attractor that will result in the drift of nearby carriers towards its vicinity. Since these carriers are trapped in QWs, this attraction from the gold NPs will result in their accumulation on the side of the well closest to the NP. The increased local concentration of carriers will not only lead to a greater number of recombinations but also accentuate the bending of the conduction and valence band (fig. 6.20), a phenomenon that as we have covered earlier is already taking place as a result of the spatially indirect nature of the nanowires' transitions. The increased band bending from the ICE will thus lead to even narrower confinement regions that in turn increases the confinement energy of the carriers causing the observed blueshift of the recombinations' energies [120].

As for the emission's intensity, no noticeable enhancement in PL seems to occur after the addition of gold nanorods to the sample contrary to what we expected and what has been previously observed in InGaN/GaN and GaAs/AlGaAs MQW systems [66]. The blueshift tells us that the nanowires are experiencing a greater accumulation of carriers on the wells' boundaries which in turn should also lead to an increase in the number of radiative recombination. As we have seen before, the strength of the ICE is dependent on the size of the NPs and the temperature. We hypothesize thus that the large dimensions of our NPs (length of 60-80 nm and width of 10-20 nm against a diameter of 17 nm and 35 nm for the NPs studied in [67], where PL enhancement was observed) on top of the high temperature (70 K) at which measurements took place, didn't allow for any considerable PL enhancement due to the greater importance of the non-radiative channels. Moreover, the process of functionalization can itself be responsible for additional non-radiative channels related with the formation of surface states.

Despite the experimental complications, our results suggest that it is possible to change the optical properties of the nanowires through their functionalization with nanorods.

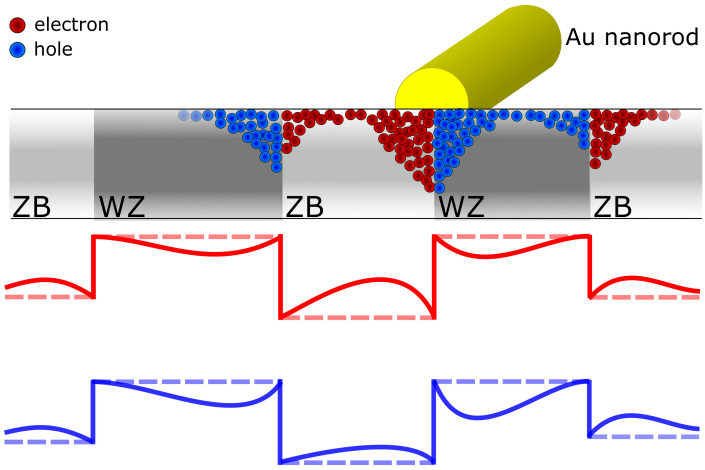


**Figure 6.20:** Illustration of how the increased local carrier concentration as a response to the Au nanoparticle leads to narrower confinement regions.

# 7 Conclusion

Throughout this work we have attempted to evaluate the physical properties of Mg-doped GaAs nanowires and the influence of the Mg doping on those properties. Moreover, the impact of gold nanorods on the optical properties was investigated. This was achieved by performing multiple optical and structural characterization techniques on two samples grown under different conditions and with different doping profiles.

Looking at our samples under a SEM showed that they comprised of a "forest" of nanowires with diameters as large as 500 nm. The different doping profiles and growth conditions of the samples had an impact on the morphology of their respective nanowires, as evidenced by the differences in the nanowires' geometry between the two. Further structural analysis of the two samples was undertaken using Raman spectroscopy. By performing it on different regions of our sample we identified WZ GaAs segments in the nanowires. With the appropriate polarization geometry, the presence or absence of a peak at around 260 $cm^{-1}$, correspondent to the $E_2^H$ vibrational mode present on WZ GaAs alone, allowed us to distinguish between the two phases. Further measurements along single nanowires revealed their polytypic nature by showing the coexistence of both phases along individual nanowires' axes.

Optical characterization of both samples was performed by PL spectroscopy. PL spectra were measured at different temperatures (from 25 K to 160 K) and at different excitation powers (from around 3 mW up to 37 mW). The most intense spectra showed obvious signs of being a superposition of different individual emissions between 1.4 eV and 1.55 eV. In an attempt to explore these emissions a model comprising five/six components was used, which allowed the deconvolution of all spectra. All but one of those bands were below the energy of the ZB GaAs bandgap. Within that model, we were able to match the emissions observed in CL at room temperature with some of the components proposed in our fitting model.

The temperature dependence of each of the considered bands varied between samples. While for one sample most of the energy vs temperature curves were typical of what is expected from semiconductors and roughly followed the ZB GaAS bandgap, the other sample showed an atypical energy curve that seems to roughly resemble the previously reported S-shaped behaviour. This hypothesis was ruled out however, as the emissions from that sample were found to have excitonic character from the power dependent PL studies, which is inconsistent with the fluctuations of potential required for the S-shaped behaviour to be present.

The different Mg doping concentration was found to be a determining factor on the radiative nature of the samples' transitions. Power dependent PL studies showed that for the sample with lower doping concentration the emissions were due to free-to-bound or donor-to-acceptor recombinations ($m < 1$), whereas for the sample with higher doping concentration the emissions owed its nature to bound exciton recombinations ($m \geq 1$).

The PL power dependency also allowed us to confirm that the recombinations in our nanowires take place across WZ/ZB or ZB/WZ interfaces, since the observed energetic blueshift with increasing power proved to be proportional to the cubic root of the excitation power for all bands but one, a dependence characteristic of spatially indirect transitions.

After the functionalization of both samples with gold nanorods no PL enhancement could be observed. Whether this was because of the large size of the NPs, the high temperatures at which measurements were performed or other physical phenomenons not considered is not clear at this point. However, a blue shift in the energy of the emission as a whole was observed as well as a change in shape which can be explained by the presence of the gold nanorods.

For future work we suggest: (i) further studies through TEM analysis, which could shed light

on the polytypic nature of the nanowires and the dimensions of the wells, (ii) time resolved spectroscopy to determine the lifetimes of the multiple emissions identified. (iii) PLE studies across the whole band of emission of the nanowires with the purpose of getting a deeper understanding of the electronic states of both samples, (iv) the improvement of the functionalization process, so as not to introduce additional non-radiative deexcitation channels that will reduce or possibly mask the nanowires' expected luminescence enhancement, (v) the use gold nanorods of smaller dimensions to test whether enhancement in luminescence is visible, and (vi) a repetition the PL experiments with more samples, each with different Mg doping concentrations, to better understand the role of Mg doping in the GaAs nanowires' luminescence.

# Bibliography


[1] Amrit De and Craig E Pryor. *Physical Review B*, 81(15):155210, 2010.

[2] Wikimedia Commons. Brillouin zone (1st, fcc), 2008.

[3] JS Blakemore. *Journal of Applied Physics*, 53(10):R123–R181, 1982.

[4] P Lautenschlager, M Garriga, S Logothetidis, and M Cardona. *Physical Review B*, 35(17):9174, 1987.

[5] Benedikt Bauer, Joachim Hubmann, Matthias Lohr, Elisabeth Reiger, Dominique Bougeard, and Josef Zweck. *Applied Physics Letters*, 104(21):211902, 2014.

[6] Bruno P Falcão, Joaquim P Leitão, Maria R Correia, Miguel F Leitão, Maria R Soares, Marcus VB Moreira, Alfredo G de Oliveira, Franklin M Matinaga, and Juan C González. *Journal of Materials Chemistry C*, 2(34):7104–7110, 2014.

[7] Katherine A Willets and Richard P Van Duyne. *Annu. Rev. Phys. Chem.*, 58:267–297, 2007.

[8] Wikimedia Commons. Molecular beam epitaxy reaction chamber, 2011.

[9] M. P. Leitão, M Sousa, Manuel Martins, B. P. Falcão, Graça Pato, Sérgio Pereira, A. G. de Oliveira, F. M. Matinaga, J. C. González, J. P. Leitão, and M. R. Correia. *Temperature dependence of Raman scattering in wurtzite GaAs nanowires: the functionalization effect with Au nanoparticles*. Poster presented at the 13th European Vacuum Conference 7th European Topical Conference on Hard Coatings, Aveiro, Portugal, 2014.

[10] Joseph Goldstein, Dale E Newbury, Patrick Echlin, David C Joy, Alton D Romig Jr, Charles E Lyman, Charles Fiori, and Eric Lifshin. *Scanning electron microscopy and X-ray microanalysis: a text for biologists, materials scientists, and geologists*. Springer Science & Business Media, 2012.

[11] Bernt KETTERER. *Raman Spectroscopy of GaAs Nanowires: Doping Mechanisms and Fundamental Properties*. PhD thesis, ÉCOLE POLYTECHNIQUE FÉDÉRALE DE LAUSANNE, 2011.

[12] I Zardo, S Conesa-Boj, F Peiro, JR Morante, J Arbiol, E Uccelli, G Abstreiter, and A Fontcuberta i Morral. *Physical Review B*, 80(24):245324, 2009.

[13] I De Wolf, J Jiménez, JP Landesman, C Frigeri, P Braun, E Da Silva, and E Calvet. Raman and luminescence spectroscopy for microelectronics. *Catalogue of optical and physical parameters."Nostradamus" project SMT4-CT-95-2024. Office for Official Publications of the European Communities, Luxembourg*, 1998.

[14] DJ Lockwood. *Journal of Solution Chemistry*, 29(10):1039–1046, 2000.

[15] Peidong Yang, Ruoxue Yan, and Melissa Fardy. *Nano letters*, 10(5):1529–1536, 2010.

[16] Allon I Hochbaum and Peidong Yang. *Chemical reviews*, 110(1):527–546, 2009.

[17] Martin Heiss, Sonia Conesa-Boj, Jun Ren, Hsiang-Han Tseng, Adam Gali, Andreas Rudolph, Emanuele Uccelli, Francesca Peiró, Joan Ramon Morante, Dieter Schuh, et al. *Physical Review B*, 83(4):045303, 2011.

[18] Vicky V Mody, Rodney Siwale, Ajay Singh, Hardik R Mody, et al. *Journal of Pharmacy and Bioallied Sciences*, 2(4):282, 2010.

[19] Matthew Pelton, Javier Aizpurua, and Garnett Bryant. *Laser & Photonics Reviews*, 2(3):136–159, 2008.

[20] Antonio Llopis. *Electrostatic Mechanism of Emission Enhancement in Hybrid Metal-semiconductor Light-emitting Heterostructures*. PhD thesis, University of North Texas, 2012.

[21] Mike Brozel. In *Springer Handbook of Electronic and Photonic Materials*, pages 499–536. Springer, 2007.

[22] Michael R Brozel and Gregory E Stillman. Number 16. IET, 1996.

[23] BP Falcão. Structural and optical characterization of Mg-doped GaAs nanowires. 2011.

[24] James R Chelikowsky and Marvin L Cohen. *Physical Review B*, 14(2):556, 1976.
[25] Sorab K Ghandhi. *VLSI fabrication principles: silicon and gallium arsenide*. John Wiley & Sons, 2008.
[26] VG Dubrovskii and NV Sibirev. *Physical Review B*, 77(3):035414, 2008.
[27] Philippe Caroff, Jessica Bolinsson, and Jonas Johansson. *Selected Topics in Quantum Electronics, IEEE Journal of*, 17(4):829–846, 2011.
[28] D Spirkoska, J Arbiol, Anders Gustafsson, Sònia Conesa-Boj, F Glas, I Zardo, M Heigoldt, MH Gass, Al L Bleloch, S Estrade, et al. *Physical Review B*, 80(24):245325, 2009.
[29] Chin-Yu Yeh, ZW Lu, S Froyen, and Alex Zunger. *Physical Review B*, 46(16):10086, 1992.
[30] Tomonori Ito. *Japanese journal of applied physics*, 37(10B):L1217, 1998.
[31] Uwe Jahn, Jonas Lähnemann, Carsten Pfüller, Oliver Brandt, Steffen Breuer, Bernd Jenichen, Manfred Ramsteiner, Lutz Geelhaar, and Henning Riechert. *Physical Review B*, 85(4):045323, 2012.
[32] Wei Zhou, Xiao-Jia Chen, Jian-Bo Zhang, Xin-Hua Li, Yu-Qi Wang, and Alexander F Goncharov. *Scientific reports*, 4, 2014.
[33] Patryk Kusch, Steffen Breuer, Manfred Ramsteiner, Lutz Geelhaar, Henning Riechert, and Stephanie Reich. *Physical Review B*, 86(7):075317, 2012.
[34] Wang Peng, F Jabeen, Bernard Jusserand, JC Harmand, and Mathieu Bernard. *Applied Physics Letters*, 100(7):073102, 2012.
[35] Michael Moewe, Linus C Chuang, Shanna Crankshaw, Chris Chase, and Connie Chang-Hasnain. *Applied Physics Letters*, 93(2):3116, 2008.
[36] F Martelli, M Piccin, G Bais, F Jabeen, S Ambrosini, S Rubini, and A Franciosi. *Nanotechnology*, 18(12):125603, 2007.
[37] Thang B Hoang, AF Moses, HL Zhou, DL Dheeraj, BO Fimland, and H Weman. *Applied physics letters*, 94(13):133105, 2009.
[38] M Murayama and T Nakayama. *Physical Review B*, 49(7):4710, 1994.
[39] Włodzimierz Nakwaski. Effective masses of electrons and heavy holes in gaas, inas, a1as and their ternary compounds. *Physica B: Condensed Matter*, 210(1):1–25, 1995.
[40] DJ Ashen, PJ Dean, DTJ Hurle, JB Mullin, AM White, and PD Greene. *Journal of Physics and Chemistry of Solids*, 36(10):1041–1053, 1975.
[41] BP Falcão, JP Leitão, JC González, MR Correia, KG Zayas-Bazán, FM Matinaga, MB Moreira, CF Leite, and AG de Oliveira. *Journal of Materials Science*, 48(4):1794–1798, 2013.
[42] N Cifuentes, ER Viana, H Limborço, DB Roa, A Abelenda, MIN da Silva, MVB Moreira, GM Ribeiro, AG de Oliveira, and JC González. *Journal of Nanomaterials*, Volume 2016, Article ID 9451319, 2016.
[43] Xiaohua Huang and Mostafa A El-Sayed. *Journal of Advanced Research*, 1(1):13–28, 2010.
[44] Partha Ghosh, Gang Han, Mrinmoy De, Chae Kyu Kim, and Vincent M Rotello. *Advanced drug delivery reviews*, 60(11):1307–1315, 2008.
[45] K Lance Kelly, Eduardo Coronado, Lin Lin Zhao, and George C Schatz. *The Journal of Physical Chemistry B*, 107(3):668–677, 2003.
[46] Otto Loebich. *Gold Bulletin*, 5(1):2–10, 1972.
[47] Ian Freestone, Nigel Meeks, Margaret Sax, and Catherine Higgitt. *Gold Bulletin*, 40(4):270–277, 2007.
[48] LA Dykman and NG Khlebtsov. *Acta Naturae ( )*, 3(2 (9)), 2011.
[49] Yuanchao Zhang, Wendy Chu, Alireza Dibaji Foroushani, Hongbin Wang, Da Li, Jingquan Liu, Colin J Barrow, Xin Wang, and Wenrong Yang. *Materials*, 7(7):5169–5201, 2014.
[50] Marco Notarianni, Kristy Vernon, Alison Chou, Muhsen Aljada, Jinzhang Liu, and Nunzio Motta. *Solar Energy*, 106:23–37, 2014.

[51] Koichi Okamoto, Isamu Niki, Alexander Shvartser, Yukio Narukawa, Takashi Mukai, and Axel Scherer. *Nature materials*, 3(9):601–605, 2004.
[52] Arup Neogi, Chang-Won Lee, Henry O Everitt, Takamasa Kuroda, Atsushi Tackeuchi, and Eli Yablonovitch. *Physical Review B*, 66(15):153305, 2002.
[53] Gustav Mie. *Contributions to the optics of turbid media, particularly of colloidal metal solutions Transl. into ENGLISH from Ann. Phys.(Leipzig), v. 25, no. 3, 1908 p 377-445*, 1:377–445, 1976.
[54] Julius Adams Stratton. Electromagnetic theory. international series in pure and applied physics, 1941.
[55] Hendrik Christoffel Hulst and HC Van De Hulst. *Light scattering by small particles*. Courier Corporation, 1957.
[56] Warren J Wiscombe. *Applied optics*, 19(9):1505–1509, 1980.
[57] William J Lentz. *Applied Optics*, 15(3):668–671, 1976.
[58] JV Dave and IBM Palo Alto Scientific Center. *Subroutines for computing the parameters of the electromagnetic radiation scattered by a sphere*. IBM Scientific Center, 1968.
[59] Jianqi Shen and Xiaoshu Cai. *PIERS Online*, 1(6):691–694, 2005.
[60] OL Muskens, P Billaud, M Broyer, N Del Fatti, and F Vallée. *Physical Review B*, 78(20):205410, 2008.
[61] Myungkoo Kang, Ali A Al-Heji, J-E Lee, Timothy W Saucer, Sunyeol Jeon, JH Wu, L Zhao, AL Katzenstein, Danielle Lee Sofferman, Vanessa Sih, et al. *Applied Physics Letters*, 103(10):101903, 2013.
[62] NE Hecker, RA Höpfel, N Sawaki, T Maier, and Gottfried Strasser. *Applied physics letters*, 75(11):1577–1579, 1999.
[63] Chu-Young Cho, Min-Ki Kwon, Sang-Jun Lee, Sang-Heon Han, Jang-Won Kang, Se-Eun Kang, Dong-Yul Lee, and Seong-Ju Park. *Nanotechnology*, 21(20):205201, 2010.
[64] Ezzat G Bakhoum. *Journal of Electrostatics*, 66(11):561–563, 2008.
[65] A Krokhin, A Neogi, A Llopis, M Mahat, L Gumen, S Pereira, and I Watson. In *Journal of Physics: Conference Series*, volume 647, page 012014. IOP Publishing, 2015.
[66] A Llopis, J Lin, SMS Pereira, T Trindade, MA Martins, IM Watson, AA Krokhin, and A Neogi. *Physical Review B*, 87(20):201304, 2013.
[67] Jie Lin, Antonio Llopis, Arkadii Krokhin, Sergio Pereira, Ian M Watson, and Arup Neogi. *Applied Physics Letters*, 104(24):242106, 2014.
[68] Qi Dai, Martin F Schubert, Min-Ho Kim, Jong Kyu Kim, EF Schubert, Daniel D Koleske, Mary H Crawford, Stephen R Lee, Arthur J Fischer, Gerald Thaler, et al. *Applied Physics Letters*, 94(11):111109, 2009.
[69] Daniel Steiauf, Emmanouil Kioupakis, and Chris G Van de Walle. *Acs Photonics*, 1(8):643–646, 2014.
[70] BA Joyce. *Reports on Progress in Physics*, 48(12):1637, 1985.
[71] Steffen Breuer. *Molecular beam epitaxy of GaAs nanowires and their suitability for optoelectronic applications*. PhD thesis, Humboldt-Universität zu Berlin, Mathematisch-Naturwissenschaftliche Fakultät I, 2012.
[72] RS Wagner and WC Ellis. *Applied Physics Letters*, 4(5):89–90, 1964.
[73] Babak Nikoobakht and Mostafa A El-Sayed. *Chemistry of Materials*, 15(10):1957–1962, 2003.
[74] Jorge Pérez-Juste, Isabel Pastoriza-Santos, Luis M Liz-Marzán, and Paul Mulvaney. *Coordination Chemistry Reviews*, 249(17):1870–1901, 2005.
[75] Danielle K Smith and Brian A Korgel. *Langmuir*, 24(3):644–649, 2008.
[76] Anand Gole and Catherine J Murphy. *Chemistry of Materials*, 16(19):3633–3640, 2004.
[77] Nikhil R Jana, Latha Gearheart, Catherine J Murphy, et al. *Advanced Materials*, 13(18):1389,

2001.

[78] *Colloids and Surfaces B: Biointerfaces*, 104:11–17, 2013.

[79] Jiang Wu, Seungyong Lee, VR Reddy, MO Manasreh, BD Weaver, MK Yakes, CS Furrow, Vas P Kunets, M Benamara, and GJ Salamo. *Materials Letters*, 65(23):3605–3608, 2011.

[80] Charles W Oatley. *Journal of Applied Physics*, 53(2):R1–R13, 1982.

[81] D McMullan. *Scanning*, 17(3):175–185, 1995.

[82] KCA Smith and CW Oatley. *British Journal of Applied Physics*, 6(11):391, 1955.

[83] Ilaria Zardo, Anna Fontcuberta i Morral, and Gerhard Abstreiter. *Raman Spectroscopy on Semiconductor Nanowires*. INTECH Open Access Publisher, 2010.

[84] S Nakashima and H Harima. Raman spectroscopy of semiconductors. *Handbook of Vibrational Spectroscopy*, 2002.

[85] Jian Wu, Duming Zhang, Qiujie Lu, Humberto R Gutierrez, and Peter C Eklund. Polarized raman scattering from single gap nanowires. *Physical Review B*, 81(16):165415, 2010.

[86] Shanna Crankshaw, Linus C Chuang, Michael Moewe, and Connie Chang-Hasnain. *Physical Review B*, 81(23):233303, 2010.

[87] CA Arguello, Denis L Rousseau, and Sérgio Pereira da Silva Porto. *Physical Review*, 181(3):1351, 1969.

[88] Thomas M Devine and Fran Adar. Raman spectroscopy of solids. *Characterization of Materials*, 2012.

[89] RS Knox. Theory of excitons in solid state physics, ed. f. seitz and d. turnbull, 1963.

[90] YU Peter and Manuel Cardona. *Fundamentals of semiconductors: physics and materials properties*. Springer Science & Business Media, 2010.

[91] Taiping Lu, Ziguang Ma, Chunhua Du, Yutao Fang, Haiyan Wu, Yang Jiang, Lu Wang, Longgui Dai, Haiqiang Jia, Wuming Liu, et al. *Scientific reports*, 4, 2014.

[92] Yatendra Pal Varshni. *Physica*, 34(1):149–154, 1967.

[93] KP O'Donnell and X Chen. *Applied Physics Letters*, 58(25):2924–2926, 1991.

[94] L Vina, S Logothetidis, and M Cardona. *Physical Review B*, 30(4):1979, 1984.

[95] R Pässler. *physica status solidi (b)*, 200(1):155–172, 1997.

[96] R Pässler. *physica status solidi(b)*, 216(2):975–1007, 1999.

[97] Gordon Davies. *Physics Reports*, 176(3):83–188, 1989.

[98] JP Leitão, A Carvalho, J Coutinho, RN Pereira, NM Santos, AO Ankiewicz, NA Sobolev, M Barroso, J Lundsgaard Hansen, A Nylandsted Larsen, et al. *Physical Review B*, 84(16):165211, 2011.

[99] BP Falcao, JP Leitão, MR Correia, MR Soares, FM Morales, JM Mánuel, R Garcia, Anders Gustafsson, MVB Moreira, AG de Oliveira, et al. *Journal of Applied Physics*, 114(18):183508, 2013.

[100] T Schmidt, K Lischka, and W Zulehner. *Physical Review B*, 45(16):8989, 1992.

[101] AM White, EW Williams, P Porteous, and C Hilsum. *Journal of Physics D: Applied Physics*, 3(9):1322, 1970.

[102] Thomas Mårtensson, C Patrik T Svensson, Brent A Wacaser, Magnus W Larsson, Werner Seifert, Knut Deppert, Anders Gustafsson, L Reine Wallenberg, and Lars Samuelson. *Nano Letters*, 4(10):1987–1990, 2004.

[103] Aarnoud L Roest, Marcel A Verheijen, Olaf Wunnicke, Stacey Serafin, Harry Wondergem, and Erik PAM Bakkers. *Nanotechnology*, 17(11):S271, 2006.

[104] A Mooradian and GB Wright. *Solid State Communications*, 4(9):431–434, 1966.

[105] S Yazji, I Zardo, M Soini, P Postorino, A Fontcuberta i Morral, and G Abstreiter. *Nanotechnology*, 22(32):325701, 2011.

[106] R Tanta, MH Madsen, Z Liao, P Krogstrup, T Vosch, Jesper Nygård, and TS Jespersen. *Applied*

*Physics Letters*, 107(24):243101, 2015.
[107] GRSK Hollinger, R Skheyta-Kabbani, and M Gendry. *Physical Review B*, 49(16):11159, 1994.
[108] PS Pizani, CEM Campos, and P Puech. *Applied Physics Letters*, 77:2924, 2000.
[109] Jacques I Pankove. *Optical processes in semiconductors*. Courier Corporation, 2012.
[110] Antonio Polimeni, M Capizzi, M Geddo, M Fischer, M Reinhardt, and A Forchel. *Applied Physics Letters*, 77(18):2870–2872, 2000.
[111] SA Lourenço, IFL Dias, JL Duarte, E Laureto, VM Aquino, and JC Harmand. *Brazilian Journal of Physics*, 37(4):1212–1219, 2007.
[112] Huining Wang, Ziwu Ji, Shuang Qu, Gang Wang, Yongzhi Jiang, Baoli Liu, Xiangang Xu, and Hirofumi Mino. *Optics express*, 20(4):3932–3940, 2012.
[113] Yong-Hoon Cho, GH Gainer, AJ Fischer, JJ Song, S Keller, UK Mishra, and SP DenBaars. *Applied Physics Letters*, 73(10):1370–1372, 1998.
[114] AM Graham, Pierre Corfdir, Martin Heiss, Sonia Conesa-Boj, Emanuele Uccelli, A Fontcuberta i Morral, and RT Phillips. *Physical Review B*, 87(12):125304, 2013.
[115] Don Monroe. *Physical review letters*, 54(2):146, 1985.
[116] Lorenzo Pavesi and Mario Guzzi. *Journal of Applied Physics*, 75(10):4779–4842, 1994.
[117] AP Levanyuk and VV Osipov. *Physics-Uspekhi*, 24(3):187–215, 1981.
[118] Masafumi Jo, Mitsuru Sato, Souta Miyamura, Hirotaka Sasakura, Hidekazu Kumano, and Ikuo Suemune. *Nanoscale research letters*, 7(1):1, 2012.
[119] G Jacopin, L Rigutti, L Largeau, F Fortuna, F Furtmayr, FH Julien, M Eickhoff, and M Tchernycheva. *Journal of Applied Physics*, 110(6):064313, 2011.
[120] YS Chiu, MH Ya, WS Su, and YF Chen. *Journal of applied physics*, 92(10):5810–5813, 2002.
[121] J Weber, W Schmid, and R Sauer. *Physical Review B*, 21(6):2401, 1980.
[122] F Luckert, MV Yakushev, C Faugeras, AV Karotki, AV Mudryi, and RW Martin. *Journal of Applied Physics*, 111(9):093507, 2012.
[123] T Hidouri, F Saidi, H Maaref, Ph Rodriguez, and L Auvray. *Optical Materials*, 62:267–272, 2016.
[124] Amlan Mukherjee, Sandip Ghosh, Steffen Breuer, Uwe Jahn, Lutz Geelhaar, and Holger T Grahn. *Journal of Applied Physics*, 117(5):054308, 2015.
[125] Bahareh Khodashenas and Hamid Reza Ghorbani. *Arabian Journal of Chemistry*, 2015.
[126] KJ Moore, P Dawson, and CT Foxon. *Physical Review B*, 38(5):3368, 1988.
[127] Donald D Fitts. 1974.
[128] Goldys and Krystyna Drozdowicz-Tomsia. *Gold and silver nanowires for fluorescence enhancement*. INTECH Open Access Publisher, 2011.
[129] Cheng-ping Huang, Xiao-gang Yin, Huang Huang, and Yong-yuan Zhu. *Optics express*, 17(8):6407–6413, 2009.
[130] Tao Jun, Lu Yong-Hua, Zheng Rong-Sheng, Lin Kai-Qun, Xie Zhi-Guo, Luo Zhao-Feng, Li Sheng-Li, Wang Pei, and Ming Hai. *Chinese Physics Letters*, 25(12):4459, 2008.
[131] NanoComposix. Gold nanorods. http://nanocomposix.com/collections/gold-nanorods. Accessed: 03-05-2016.
[132] NanoComposix. Gold nanoparticles: Optical properties. http://nanocomposix.com/pages/gold-nanoparticles-optical-properties. Accessed: 03-05-2016.
[133] Federico Jose Williams and Maria Joselevich. Diazonium functionalized nanoparticles and methods for binding nanoparticles to metallic surfaces, August 7 2012. US Patent 8,236,422.
[134] Kyeong-Seok Lee and Mostafa A El-Sayed. *The Journal of Physical Chemistry B*, 110(39):19220–19225, 2006.
[135] Brantley D Busbee, Sherine O Obare, and Catherine J Murphy. *Advanced Materials*,

15(5):414–416, 2003.
[136] Gaoxing Su, Chi Yang, and Jun-Jie Zhu. *Langmuir*, 31(2):817–823, 2015.
[137] Brian G McMillan, Léonard EA Berlouis, Francis R Cruickshank, David Pugh, and Pierre-François Brevet. *Applied Physics Letters*, 86(21):211912, 2005.
[138] Jun Ge, Jiandu Lei, and Richard N Zare. *Nature nanotechnology*, 7(7):428–432, 2012.
[139] Andrew J Frank, Nicole Cathcart, Kenneth E Maly, and Vladimir Kitaev. *Journal of chemical education*, 87(10):1098–1101, 2010.
[140] Anastassios Mavrokefalos, Sang Eon Han, Selcuk Yerci, Matthew S Branham, and Gang Chen. *Nano letters*, 12(6):2792–2796, 2012.
[141] Guijun Li, He Li, Jacob YL Ho, Man Wong, and Hoi Sing Kwok. *Nano letters*, 14(5):2563–2568, 2014.
[142] HD Sun, M Hetterich, MD Dawson, A Yu Egorov, D Bernklau, and H Riechert. *Journal of applied physics*, 92(3):1380–1385, 2002.
[143] Hannah J Joyce, Qiang Gao, H Hoe Tan, Chennupati Jagadish, Yong Kim, Jin Zou, Leigh M Smith, Howard E Jackson, Jan M Yarrison-Rice, Patrick Parkinson, et al. *Progress in Quantum Electronics*, 35(2):23–75, 2011.
[144] L Grenouillet, C Bru-Chevallier, G Guillot, P Gilet, P Duvaut, C Vannuffel, A Million, and A Chenevas-Paule. *Applied Physics Letters*, 76(16):2241, 2000.
[145] A Kaschner, T Lüttgert, H Born, A Hoffmann, A Yu Egorov, and H Riechert. *Applied Physics Letters*, 78(10):1391–1393, 2001.
[146] E Kuokstis, J Zhang, M-Y Ryu, JW Yang, Grigory Simin, M Asif Khan, R Gaska, and MS Shur. *Applied Physics Letters*, 79(26):4375–4377, 2001.
[147] Thomas Andre Karlberg. Optical studies of single semiconductor nanowires by micro-photoluminescence spectroscopy. 2010.
[148] Ewen Smith and Geoffrey Dent. *Modern Raman spectroscopy: a practical approach*. John Wiley & Sons, 2013.
[149] Priyanka Bhoyar and SJ Dhoble. *Materials Chemistry and Physics*, 140(1):104–107, 2013.
[150] Bernt Ketterer, Martin Heiss, Emanuele Uccelli, Jordi Arbiol, and Anna Fontcuberta i Morral. *ACS nano*, 5(9):7585–7592, 2011.
[151] PP Paskov, R Schifano, Bo Monemar, T Paskova, S Figge, and D Hommel. *Journal of Applied Physics*, 98(9):93519–93519, 2005.
[152] Pierre Corfdir, Pierre Lefebvre, Jacques Levrat, Amélie Dussaigne, J-D Ganière, Denis Martin, Jelena Ristic, Tiankai Zhu, Nicolas Grandjean, and Benoît Deveaud-Plédran. *Journal of Applied Physics*, 105(EPFL-ARTICLE-174834):043102, 2009.
[153] S Yang, CC Kuo, W-R Liu, BH Lin, H-C Hsu, C-H Hsu, and WF Hsieh. *Applied Physics Letters*, 100(10):101907, 2012.
[154] Pierre Corfdir and Pierre Lefebvre. *Journal of Applied Physics*, 112(5):053512, 2012.